

1  
2 **Timing and provenance of volcanic fluxes around the Permian-Triassic Boundary**  
3 **Mass Extinction in South China: U-Pb zircon geochronology, volcanic ash**  
4 **geochemistry and mercury isotopes**

5 **Oluwaseun Edward<sup>1</sup>, André Navin Paul<sup>2</sup>, Hugo Bucher<sup>3</sup>, Christian Vérard<sup>2</sup>, Thierry**  
6 **Adatte<sup>4</sup>, Jeroen E. Sonke<sup>5</sup>, Urs Schaltegger<sup>2</sup>, Torsten Vennemann<sup>1</sup>**

7 <sup>1</sup>Institute of Earth Surface Dynamics, Géopolis, University of Lausanne, CH-1015 Lausanne,  
8 Switzerland

9 <sup>2</sup>Department of Earth Sciences, Université de Genève, Rue des Maraîchers 13, CH-1205 Genève

10 <sup>3</sup>Paläontologisches Institut der Universität Zürich, Karl-Schmid-Strasse 4, 8006 Zürich,  
11 Switzerland

12 <sup>4</sup>Institute of Earth Sciences, Géopolis, University of Lausanne, CH-1015 Lausanne, Switzerland

13 <sup>5</sup>Observatoire Midi-Pyrénées, Géosciences Environnement Toulouse, Université Paul Sabatier  
14 Toulouse 3, 14 Avenue Edouard Belin, 31400 Toulouse, France

15 Corresponding author: Oluwaseun Edward ([oluwaseun.edward@unil.ch](mailto:oluwaseun.edward@unil.ch))

16 **Key Points:**

- 17 • Mercury concentrations show elevated volcanic fluxes to South China before and after  
18 the Permian-Triassic boundary.
- 19 • The recorded mercury anomalies are attributed primarily to regional subduction-related  
20 arc volcanism, not the Siberian Traps.
- 21 • Our data provide evidence that regional arc volcanism contributed to mass extinction in  
22 South China during the Permian-Triassic transition.

## 23 Abstract

24 Anomalous mercury (Hg) contents recorded near the Permian-Triassic boundary (PTB) are often  
25 linked to Siberian Traps Large Igneous Province (STLIP) volcanism and the Permian-Triassic  
26 boundary mass extinction (PTBME). However, mounting evidence indicates that the relation  
27 between STLIP volcanism and Hg “anomalies” is not straightforward. This study focuses on the  
28 timing and provenance of volcanic fluxes around the PTBME in South China. We constrain  
29 carbon isotope ( $\delta^{13}\text{C}$ ) and Hg concentration and isotope records by utilizing high-precision U-Pb  
30 zircon ages from two expanded deep-water marine sections spanning the Late Permian to Early  
31 Triassic in the Nanpanjiang Basin. Results reveal two episodes of Hg enrichment. The oldest  
32 episode predates the onset of a large negative  $\delta^{13}\text{C}$  excursion, which is documented to be older  
33 than  $252.07 \pm 0.130$  Ma. The second episode occurred between  $251.822 \pm 0.060$  Ma and  $251.589$   
34  $\pm 0.062$  Ma, coinciding with the nadir of the  $\delta^{13}\text{C}$  excursion. Volcanic ash geochemistry and Hg  
35 isotope compositions suggest that mercury was sourced from subduction-related volcanic arc  
36 magmatism in the Tethys region, which peaked between  $251.668 \pm 0.079$  Ma and  $251.589 \pm$   
37  $0.052$  Ma. These results support the hypothesis that regional arc volcanism contributed to the  
38 causes of the PTBME in South China and provide evidence that Hg anomalies close to the PTB  
39 are not a reliable stratigraphic marker for the PTB extinction event. This study demonstrates that  
40 the relations between volcanism, environmental perturbations and mass extinction during the  
41 Permian-Triassic transition are better resolved with the aid of high-precision U-Pb zircon ages.

## 42 Plain Language Summary

43 Unusually high mercury contents in sedimentary rock sequences and the mass extinction of  
44 organisms during the transition from the Permian–Triassic Period are often linked to Siberian  
45 Traps volcanism. However, results from several studies indicate that the relationship between  
46 this massive volcanism and mercury peaks in Permian- to Triassic-aged rocks in the South China  
47 region is complex. This study combines the geochemical and isotopic records of carbon and  
48 mercury from Late Permian to Early Triassic sedimentary rocks, with absolute ages determined  
49 from interlayered volcanic ashes, to investigate the presence, timing, and source of volcanic  
50 inputs to these rock successions in South China. Results show higher mercury concentrations in  
51 two intervals, one before and after the Permian-Triassic boundary. Absolute age results indicate  
52 that the mercury peak closest to the Permian-Triassic boundary occurred around 300,000 years  
53 after the mass extinction. We attribute the mercury peaks to more local volcanic activity than the  
54 far away Siberian Traps and suggest that this regional-scale volcanic activity began shortly  
55 before 252 million years ago (Ma) and peaked around 251.6 Ma. Our results support suggestions  
56 that regional volcanism played a significant role in causing mass extinction in the South China  
57 region around 251.9 Ma.

## 58 1 Introduction

59 The Paleozoic – Mesozoic transition (ca. 252 million years ago) was characterized by the  
60 largest mass extinction event in the Phanerozoic – the Permian-Triassic boundary mass  
61 extinction (PTBME), which paved the way for the faunal transition from the Paleozoic  
62 evolutionary fauna to the modern fauna (Dal Corso et al., 2022). Furthermore, major  
63 perturbations of the global carbon and mercury cycles (expressed as negative carbon (C) isotope  
64 excursions and mercury (Hg) concentration spikes, respectively) are documented for sedimentary  
65 successions straddling the Permian-Triassic boundary (PTB) in several spatially disparate  
66 localities (e.g., Baud et al., 1989; 1996; Korte & Kozur, 2010; J. Shen et al., 2019; S. Shen et al.,

67 2013; Sial et al., 2020). Causal mechanisms for the extinction are still debated. However, the  
68 most popular trigger suggested by researchers is the temporally overlapping volcanic activity of  
69 the Siberian Large Igneous Province (STLIP), based on a temporal overlap between intrusive  
70 STLIP magmatism and the extinction interval at the Meishan Global Stratotype Section and  
71 Point (GSSP) (Burgess & Bowring, 2015; Burgess et al., 2017).

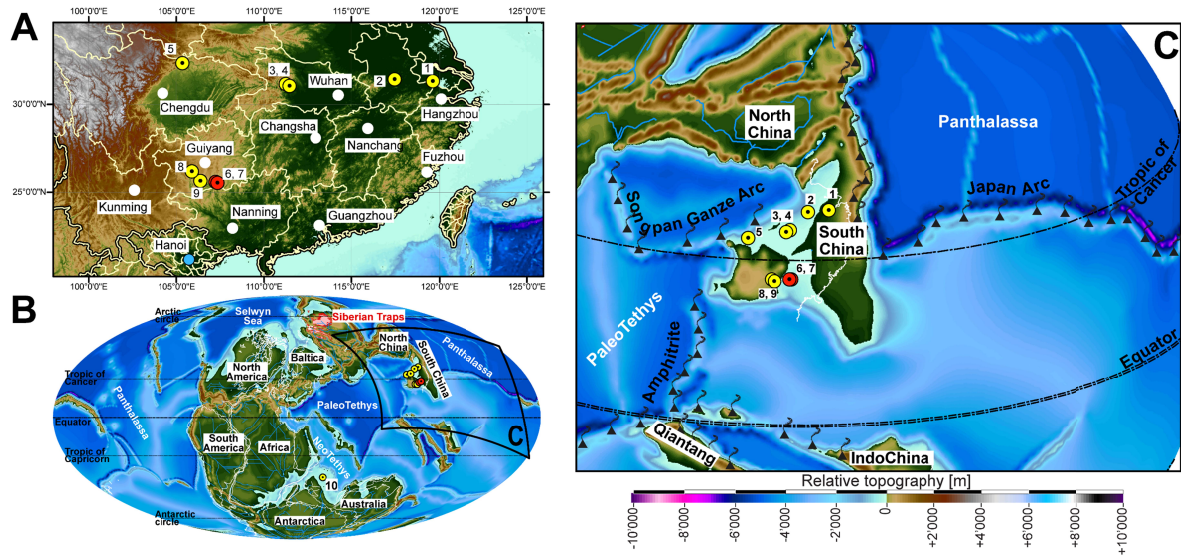
72 The connection between volcanic activity and Hg concentration spikes in sedimentary  
73 successions is founded on the understanding that volcanoes are the dominant natural source of  
74 Hg to the environment (Pyle & Mather, 2003). As such, LIP volcanism could result in the  
75 emission and sequestration of high levels of Hg in the environment. Consequently, mercury  
76 “anomalies” – relatively high Hg concentrations or Hg/TOC ratios in a portion of strata within a  
77 given sedimentary succession – are used to trace the timing of Large Igneous Province (LIP)  
78 magmatism in the geological record (e.g., Yager et al., 2021). In the case of the  $\delta^{13}\text{C}$  record,  
79 previous studies have interpreted the negative C isotope excursion associated with the PTB as the  
80 result of the intrusion of magma into surrounding organic-rich country rocks (e.g., coal) in the  
81 Tunguska Basin, Siberia, introducing significant amounts of isotopically light C into the ocean-  
82 atmosphere system (Broadley et al., 2018; Svensen et al., 2009). Thus, Hg anomalies and  
83 negative  $\delta^{13}\text{C}$  excursions recorded close to the PTB are usually interpreted in the context of  
84 STLIP volcanism and its associated deleterious environmental effects leading to faunal  
85 extinction.

86 However, our understanding of the links between STLIP volcanism, carbon cycle  
87 perturbations and mass extinction during the Permian-Triassic transition are still complicated by  
88 several factors. First, Hg and Hg/TOC content vary significantly near the PTB between different  
89 localities and the relative timing of Hg anomalies with regards to the PTBME horizon is  
90 inconsistent (e.g., J. Shen et al., 2019; Sial et al., 2020; Wang et al., 2018). In addition, Hg  
91 anomalies can also be influenced by factors other than direct volcanic emissions. For instance,  
92 Hg anomalies can arise from increased input of Hg remobilized from soils to marine sediments  
93 due to increased erosion and continental weathering rates, and sedimentary Hg records can be  
94 distorted by post-depositional weathering, erosion, and thermal alteration (Charbonnier et al.,  
95 2020; Chen et al., 2022). Second, the correlation of geochemical records between different  
96 localities is fraught with uncertainty because the position of the PTB in many successions  
97 remains uncertain (e.g., Johnson et al., 2021; J. Shen et al., 2019; Sial et al., 2020); and  
98 sedimentary and volcanic successions straddling the Permian and Triassic are often characterized  
99 by an unconformity at the PTB (Burgess & Bowring, 2015; Davydov, 2021; Yin et al., 2014),  
100 which for South China has been estimated to represent a time gap of about  $89 \pm 38$  kyr for the  
101 Permian part (Baresel et al., 2017a). Third, it has become apparent that several paleocontinents,  
102 including South China, experienced extensive regional intermediate to felsic volcanism during  
103 the Permian-Triassic transition (Gao et al., 2013; J. Shen et al., 2021; Vajda et al., 2020; H.  
104 Zhang et al., 2021), increasing the potential sources of volcanic Hg input to PTB marine records  
105 at these localities. Fourth, absolute time calibration of the eruptive history of the STLIP remains  
106 coarse, limiting precise temporal correlations between STLIP magmatism and mass extinction  
107 (Dal Corso et al., 2022), although, U-Pb geochronologic evidence suggests that the PTBME may  
108 have been limited to only a short period of STLIP magmatism (Burgess et al., 2017).  
109 Consequently, considering the complex biogeochemical cycling of Hg, the widespread  
110 incompleteness of the PTB rock record (which limits the accuracy of chemostratigraphic and  
111 biostratigraphic correlations and the placement of the PTB), and the occurrence of more  
112 proximal regional volcanic activity capable of locally supplying Hg, links between Hg anomalies

113 around the PTB and STLIP magmatism cannot be unequivocally inferred without a thorough  
114 assessment of the provenance of the recorded Hg anomalies and their timing relative to the  
115 PTBME using precise and accurate geochronology.

116 Hg isotopes are widely used to trace the sources of Hg anomalies in ancient sedimentary  
117 successions, as different transformations during the biogeochemical cycling of Hg can induce  
118 mass-dependent (MDF) and/or mass-independent fractionation (MIF) of Hg isotopes (Blum et  
119 al., 2014; Thibodeau & Bergquist, 2017). Previous studies have applied Hg isotopes in  
120 investigating the source of Hg anomalies and its relationship to the PTBME in Permian-Triassic  
121 successions of South China and elsewhere (Grasby et al., 2017; J. Shen et al., 2021; J. Shen et  
122 al., 2019; Wang et al., 2019a; Wang et al., 2018). However, these studies have provided mixed  
123 results, with Hg MIF data from nearshore depositional settings reflecting a dominant terrestrial  
124 Hg source and those from deeper-water depositional settings being congruent with atmospheric  
125 volcanic Hg input (Grasby et al., 2017; Wang et al., 2018). Hence, it has been suggested that the  
126 Hg isotope record for these successions mostly reflects their depositional setting (Yager et al.,  
127 2021) and that deep-water marine sections, being less vulnerable to terrestrial Hg inputs, may be  
128 better suited for investigations of volcanic Hg input sources (Grasby et al., 2017; Thibodeau &  
129 Bergquist, 2017; Wang et al., 2018).

130 The Upper Permian to Lower Triassic of South China is characterized by the widespread  
131 occurrence of volcanic ash layers (Gao et al., 2013; He et al., 2014; Yang et al., 2012),  
132 permitting precise and accurate U-Pb zircon geochronological calibrations of Permian-Triassic  
133 successions (e.g., Baresel et al., 2017a, 2017b; Burgess et al., 2014; Lehrmann et al., 2015; S.  
134 Shen et al. 2019), as well as providing a means of evaluating the provenance of volcanic  
135 products (e.g. zircon) to sedimentary successions in South China (e.g., Jiao et al., 2022; Zhao et  
136 al., 2019). However, except for the Shangsi section (S. Shen et al., 2011), Hg anomalies recorded  
137 near the PTB from deep-water marine settings in South China lack U-Pb zircon age calibration.  
138 Also, the published U-Pb zircon ages for Shangsi were not obtained with the most recent  
139 EARTHTIME spike (Yuan et al., 2019), which makes a direct comparison with ages obtained  
140 using this spike problematic at high temporal resolution. In addition to enabling precise  
141 geochronology, volcanic ashes provide an archive for the assessment of magmatic sources, as  
142 their geochemical compositions reflect those of the source magma (e.g., He et al., 2014; Song et  
143 al., 2022; Yang et al., 2012). This study presents, for the first time, a paired  $\delta^{13}\text{C}$  and Hg  
144 (concentration and isotope) record calibrated by precise and accurate U-Pb zircon ages from two  
145 sections (Laxian and Potuo) representing deep-water marine depositional environments in the  
146 Nanpanjiang Basin, South China. The aim of the study is to assess the occurrence, timing and  
147 provenance of volcanic fluxes during the Permian-Triassic transition in South China.



148

149 **Figure 1.** a) Map showing the present-day location of the studied sections (red circles) and other  
 150 deep-water marine sections in South China (yellow circles); white circles show the main cities.  
 151 The sections are represented by numbers as follows: 1 – Meishan, 2 – Majiashan, 3 – Daxiakou,  
 152 4 – Xiakou. 5 – Shangsi, 6 – Laxian, 7 – Potuo, 8 – Xinmin, 9 – Kejiao b) Global  
 153 paleogeographic map at the Permian-Triassic transition after the Panalesis model (Vérard, 2019).  
 154 Locality marked ‘10’ represents the paleo-location of Guryul Ravine, northern India. c) Detailed  
 155 map of the South China area (orthogonal projection) with the paleo-location of the discussed  
 156 sections.

157

### 1.1 Geological Context

158 The Potuo and Laxian sections (Fig. 1) are situated in the NE-SW trending Pingtang  
 159 syncline, which in the present-day, is in the northern part of the Nanpanjiang Basin, South China  
 160 (Bagherpour et al. 2020). The Changhsingian (Late Permian) sedimentary succession in Potuo is  
 161 characterized by thin-bedded siliceous mudstones interbedded with volcanic ash layers: the  
 162 Talung Formation. The Griesbachian (Induan, Early Triassic) consists of laminated black shales  
 163 with interbedded concretionary micritic limestones and occasional ash beds representing the  
 164 Daye Formation. The Changhsingian to Griesbachian sedimentary succession for Laxian is  
 165 similar to that of Potuo except that there are no concretionary micritic limestone beds  
 166 interbedded with the Griesbachian shale units. The Late Permian to Early Triassic sedimentary  
 167 sequence in these localities is interpreted to have been deposited as a continuous section in a  
 168 deep-water basin paleoenvironment, hence without an unconformity between the Talung and  
 169 Daye formations (Bagherpour et al., 2020). As such, these sections are ideally suited for our  
 170 combined geochronologic and geochemical study, having been deposited in troughs within a  
 171 horst-and-graben paleotopography (Bagherpour et al., 2020). In addition, the presence of  
 172 volcanic ashes in these sections enables studies of latest Permian to earliest Triassic volcanic  
 173 fluxes to the Nanpanjiang Basin of South China. Samples spanning the Upper Permian to Lower  
 174 Triassic used for this study are the same as those analyzed by Bagherpour et al. (2020) and  
 175 details on the geological setting, lithostratigraphy, biostratigraphy, as well as  $\delta^{13}\text{C}$  record for  
 176 these sections are given in that study.

## 177 2 Materials and Methods

178 For this study, measurements of the Hg concentrations (n=70) and isotopic compositions  
179 (n=22), total organic carbon (TOC) contents (n=54), major and trace element concentrations for  
180 sedimentary rocks (n=49) and interbedded volcanic ash beds (n=6) were made. This was  
181 complemented by U-Pb zircon geochronology based on single zircon grains from five volcanic  
182 ash beds in the two sections (Table S1, supplementary information).

### 183 2.1 Stratigraphical correlation of the study sections

184 Stratigraphical correlation between the two sections studied – Laxian (25.78880°N,  
185 107.29750°E) and Potuo (25.82638°N, 107.24861°E) follows Bagherpour et al. (2020). The PTB  
186 is delineated based on the conformable lithostratigraphic boundary between the Talung and Daye  
187 formations, which for deep-water sections of the Nanpanjiang Basin, has been shown to be  
188 equivalent to the PTB as defined at the Meishan D GSSP based on U-Pb zircon ages (Burgess et  
189 al., 2014; Baresel et al., 2017b). The stratigraphical correlation of the Laxian and Potuo sections  
190 by Bagherpour et al. (2020) is further confirmed by the Hg chemostratigraphy and U-Pb zircon  
191 ages of this study (see section 3).

### 192 2.2 Mercury concentration and isotopic composition

193 Mercury concentration was measured using a Zeeman R-915F high-frequency atomic  
194 absorption spectrometer at the University of Lausanne, Switzerland. Samples (sedimentary  
195 rocks, including volcanic ashes) were analyzed in triplicates to ensure analytical precision and  
196 the reference material – GSD-11, Chinese alluvium (Hg concentration of  $72 \pm 9$  ppb; Zintwana et  
197 al., 2012) was used to monitor accuracy of the measurements (correlation coefficient = 0.99,  
198 standard residual deviation = 5 %).

199 Twenty-two samples (Potuo = 11, Laxian = 11) with sufficiently high Hg concentrations  
200 ( $\geq 9$  ppb) were selected for Hg isotopic analysis at the Observatoire Midi-Pyrénées, Toulouse,  
201 France. Mercury was preconcentrated using a double-stage tube furnace – acid-trapping protocol  
202 as detailed by Sun et al. (2013). Powdered samples were loaded in quartz tubes (pre-cleaned at  
203 550 °C), capped at both ends with quartz wool and heated in a combustion furnace connected to  
204 a flow of Hg-free oxygen and set to ramp up from room temperature to 900 °C within 6 hours.  
205 Liberated gaseous Hg<sup>0</sup> was then purged into a decomposition oven, held at 1000 °C, using a  
206 continuous flow of oxygen. Subsequently, the Hg<sup>0</sup> was collected by oxidation to Hg<sup>II</sup> in a  
207 trapping solution of 40 % (v/v) inverse aqua regia (iAR, 2HNO<sub>3</sub>/1HCl), which was then diluted  
208 at the end of the 6 h pre-concentration to 20 % (v/v) iAR and stored at 4 °C in the dark before Hg  
209 isotopic measurements (Sun et al., 2013). Two certified reference materials, NIST 1632D  
210 (bituminous coal, n=2) and MESS3 (Arctic marine sediment, n=2) were processed along with the  
211 samples. Hg isotope compositions were subsequently measured in duplicate over two analytical  
212 sessions by cold vapor multi-collector inductively coupled plasma mass spectrometry (CV-MC-  
213 ICPMS) following analytical procedures detailed by Sonke et al., 2010; Sun et al., 2013 and  
214 Jiskra et al., 2021. Briefly, the Hg<sup>II</sup> in the iAR trap solution was reduced to Hg<sup>0</sup> vapor using  
215 SnCl<sub>2</sub> solution (3 %, w/v, in 1 M HCl) and then analyzed for Hg stable isotopes using an online  
216 CETAC HGX-200 cold vapor generator coupled to a Thermo-Scientific Neptune PLUS<sup>TM</sup>  
217 equipped with a 10<sup>12</sup> Ω resistor on the <sup>198</sup>Hg isotope. The MC-ICPMS instrumental mass bias  
218 was corrected by sample-standard bracketing using the NIST 3133 standard at matching standard  
219 and sample concentrations (0.71 ppb and 2.1 ppb). Long-term instrumental precision was

220 monitored by repeated analysis of the ETH-Fluka (n = 6) and UM-Almaden (n = 3) Hg standard  
 221 solutions at Hg concentrations corresponding to the samples (i.e., 0.71 ng/g and 2.1 ng/g).  
 222 Procedural blanks had an average Hg concentration of ~ 0.01 ng/g (n=3). Mass-dependent  
 223 fractionation (MDF) of Hg isotopes is reported in small delta notation ( $\delta$ ) as  $\delta^{202}\text{Hg}$  in permil  
 224 (‰) relative to the bracketing NIST 3133 standard:

$$225 \quad \delta^{202}\text{Hg} = [((^{202}\text{Hg}/^{198}\text{Hg})_{\text{sample}} / (^{202}\text{Hg}/^{198}\text{Hg})_{\text{NIST3133}} - 1) \times 10^3] \quad (1)$$

226 Mass independent fractionation (MIF) values are denoted using capital delta ( $\Delta$ ) notation and are  
 227 defined as the difference between the measured values of  $\delta^{199}\text{Hg}$ ,  $\delta^{200}\text{Hg}$ ,  $\delta^{201}\text{Hg}$ ,  $\delta^{204}\text{Hg}$  and  
 228 those predicted for MDF with respect to  $\delta^{202}\text{Hg}$  using the kinetic MDF law as follows:

$$229 \quad \Delta^{\text{xxx}}\text{Hg} = \delta^{\text{xxx}}\text{Hg} - K_{\text{xxx}} \times \delta^{202}\text{Hg} \quad (2)$$

230 where xxx refers to Hg isotope masses 199, 200, 201, and 204, and  $K_{\text{xxx}}$  refers to the constants  
 231 that are used to calculate values for  $\Delta^{\text{xxx}}\text{Hg}$ , which are: 0.2520, 0.5024, 0.7520 and 1.4930 for  
 232  $\delta^{199}\text{Hg}$ ,  $\delta^{200}\text{Hg}$ ,  $\delta^{201}\text{Hg}$  and  $\delta^{204}\text{Hg}$  respectively (Blum & Bergquist, 2007). Hg isotopic  
 233 compositions are reported as the mean of duplicate measurements and analytical uncertainty of  
 234 isotopic analysis are reported conservatively, as either the  $2\sigma$  ( $2 \times$  standard deviation) of the  
 235 replicate sample measurements or that of the standard with the largest  $2\sigma$ , whichever was larger.  
 236 ETH-Fluka and UM-Almaden standard solutions yielded mean values ( $\pm 2\sigma$ ) of  $-1.48 \pm 0.14$  ‰,  
 237  $0.09 \pm 0.03$  ‰,  $0.04 \pm 0.03$  ‰,  $0.04 \pm 0.07$  ‰; and  $-0.59 \pm 0.09$  ‰,  $-0.03 \pm 0.10$  ‰,  $0.02 \pm 0.06$   
 238 ‰ and  $-0.05 \pm 0.07$  ‰ for  $\delta^{202}\text{Hg}$ ,  $\Delta^{199}\text{Hg}$ ,  $\Delta^{200}\text{Hg}$ , and  $\Delta^{201}\text{Hg}$  respectively. NIST 1632D and  
 239 MESS-3 had mean values of  $-1.93 \pm 0.32$  ‰,  $-0.01 \pm 0.05$  ‰,  $-0.06 \pm 0.08$  ‰,  $-0.06 \pm 0.01$  ‰;  
 240 and  $-2.25 \pm 0.02$  ‰,  $0 \pm 0.04$  ‰,  $0.04 \pm 0.03$  ‰ and  $-0.14 \pm 0.14$  ‰ for  $\delta^{202}\text{Hg}$ ,  $\Delta^{199}\text{Hg}$ ,  $\Delta^{200}\text{Hg}$ ,  
 241 and  $\Delta^{201}\text{Hg}$  respectively. These mean values are comparable with reported values for these  
 242 standard solutions and certified reference materials (Jiskra et al., 2019; Kwon et al., 2015; Sun et  
 243 al., 2013).

### 244 2.3 Organic carbon content

245 All total organic carbon (TOC) content data for Laxian (n=26) were acquired during the  
 246 present study. For the Potuo section, 10 data points are from Bagherpour et al. (2020) and an  
 247 additional 28 samples have been analyzed for this study. Organic matter content and preservation  
 248 was assessed by Rock-Eval pyrolysis using a Rock Eval<sup>TM</sup> 6 with the analytical procedures  
 249 described by Behar et al. (2001). This included measurements of total organic carbon (TOC)  
 250 content, hydrogen index (HI) and oxygen index (OI). The standard IFP160000 was used for  
 251 calibration of the samples and instrumental precision was about 0.1 wt.% for TOC, 10 mg HC/g  
 252 for HI and 10 mg CO<sub>2</sub>/g for OI.

### 253 2.4 Major and trace element analysis

254 Major and trace element concentrations were analyzed by X-ray fluorescence (XRF)  
 255 spectrometry on glass discs and pressed tablets, respectively, using a PANalytical PW2400 XRF  
 256 spectrometer at the University of Lausanne, Switzerland. The standard reference materials: JLS-  
 257 1, JDO-1 and BHVO were used for assessment of analytical accuracy. External reproducibility  
 258 ( $1\sigma$ ) is between 0.5 % and 5 % depending on the element, and detection limit for major elements  
 259 is ca. 0.01 % and between 1 and 7 ppm for trace elements.

### 260 2.5 U-Pb zircon geochronology

261 In total, nine volcanic ash layers from the Talung (Late Permian) and Daye (Early  
 262 Triassic) formations at Potuo (POT66T, POT67T, and POT68T) and Laxian (LAX8T, LAX9T,

263 LAX10T, LAX11T, LAX 13T and LAX14T) were processed for U-Pb zircon dating. Of these,  
264 seven ash layers yielded sufficient zircon crystals for CA ID-TIMS U-Pb analyses. Zircon U-Pb  
265 isotopic compositions were determined by chemical abrasion, isotope dilution, thermal ionization  
266 mass spectrometry (CA-ID-TIMS) at the University of Geneva, Switzerland, following the  
267 procedure described by Widmann et al. (2019). Zircons were extracted from ash beds by  
268 conventional methods (crushing, milling, sieving, magnetic and density separation), including  
269 hand-picking of high aspect ratio grains free of visible inclusions. The zircon grains were  
270 thermally treated at 900 °C for 48 h to stimulate self-annealing prior to partial dissolution in  
271 concentrated hydrofluoric acid ( $\text{HF}_{\text{conc}}$ ), to remove structurally damaged domains that may have  
272 suffered lead (Pb) loss (see Widmann et al. (2019) for the detailed procedure). The partially  
273 dissolved grains were then extracted and washed in 6N HCl in 3 ml Savillex beakers overnight  
274 (min. 12 h), at 80 °C. Further cleaning steps involve cycling of 7N  $\text{HNO}_3$  and ultra-sonic bathing  
275 prior to loading into 200  $\mu\text{l}$  capsules for dissolution in 2 to 3 drops of  $\text{HF}_{\text{conc}}$  for 48 h at 210 °C in  
276 pressurized Parr<sup>TM</sup> vessels. A  $^{202}\text{Pb}$ - $^{205}\text{Pb}$ - $^{233}\text{U}$ - $^{235}\text{U}$  tracer solution: ET2535 (EARTHTIME  
277 2535, Condon et al., 2015) was added prior to dissolution, and Pb and U were isolated using ion  
278 exchange resin chromatography. Uranium and Pb isotopic compositions were measured on an  
279 IsotopX Phoenix TIMS at the University of Geneva. Pb was measured using a dynamic peak  
280 jumping routine on a Daly ion counting system, while uranium was measured as  $\text{UO}_2$  in static  
281 mode using  $10^{12} \Omega$  resistor Faraday amplifiers for samples POT66T, POT67T, POT68T, and  
282 using ATONA Faraday amplifiers (with a 30 s integration time) for samples LAX8T and  
283 LAX10T. The measured isotopic ratios were corrected for interferences of  $^{238}\text{U}^{18}\text{O}^{16}\text{O}$  on  
284  $^{235}\text{U}^{16}\text{O}_2$  using a  $^{18}\text{O}/^{16}\text{O}$  composition of 0.00205 based on repeat measurements of the U500  
285 standard. Mass fractionation of U was corrected using a double isotope tracer with a  $^{235}\text{U}/^{233}\text{U}$  of  
286  $0.99506 \pm 0.005$ . The Pb blank isotopic composition is  $^{206}\text{Pb}/^{204}\text{Pb} = 17.43 \pm 0.71$  ( $1\sigma$ ),  
287  $^{207}\text{Pb}/^{204}\text{Pb} = 14.73 \pm 0.38$  ( $1\sigma$ ) and  $^{208}\text{Pb}/^{204}\text{Pb} = 35.58 \pm 1.04$  ( $1\sigma$ ), based on total procedural  
288 blank measurements.

289 U-Pb dates of zircons were calculated using data reduction software Tripoli and ETRedux  
290 (Bowring et al., 2011; McLean et al., 2011)), and all uncertainties are reported at the 95 %  
291 confidence interval. The interpreted weighted mean age is reported in the format: “weighted  
292 mean”  $\pm$  /X/Y/Z, where X corresponds to analytical uncertainty, Y to analytical + tracer  
293 uncertainty and Z to analytical, tracer and decay constant uncertainty (Schoene et al., 2006). All  
294 zircon  $^{206}\text{Pb}/^{238}\text{U}$  dates were corrected for  $^{230}\text{Th}$ - $^{238}\text{U}$  disequilibrium using a  $\text{Th}/\text{U}_{\text{magma}}$  of  $3.5 \pm$   
295  $1.0$ . We discuss dates at the precision level of analytical uncertainty (X), since most U-Pb data in  
296 the relevant literature were obtained using the same isotope tracer (ET2535) and mode of  
297 analysis (ID-TIMS), effectively eliminating inter-lab uncertainty. Repeat analyses of the ET100  
298 solution ( $^{206}\text{Pb}/^{238}\text{U}$  date:  $100.173 \pm 0.003$  Ma; Schaltegger et al., 2021) yielded a value of  
299  $100.1338 \pm 0.0090$  Ma (MSWD = 3.2, n = 11). Excess scatter is indicated by the elevated  
300 MSWD value and is commonly observed for the synthetic ET100 solution. This is potentially  
301 derived from instrument instability and from the sample preparation process. In Schaltegger et al.  
302 (2021), systematic variation of the ET100 weighted mean age was explained by minor U/Pb  
303 fractionation over time due to spike bottle depletion. The spike bottle level used in this study was  
304  $< 20$  % of its original volume, which could possibly explain part of the deviation from the May  
305 2020 Geneva average ET100 value of  $100.167 \pm 0.009$  (Schaltegger et al., 2021). However, any  
306 intra-sample ET2535 long term fractionation variation is expected to be  $< 0.1$  % of the  $^{206}\text{Pb}/^{238}\text{U}$   
307 date and would affect the zircons analyzed in this study equally.

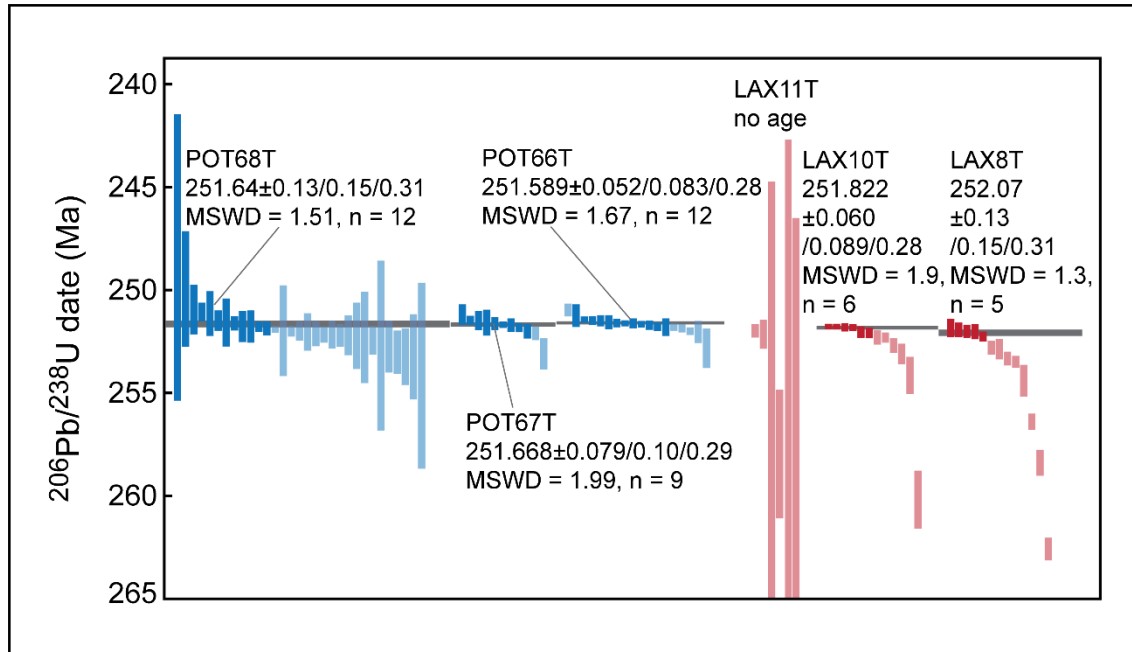
308 **3 Results**

309 Results of all geochemical analyses are given in the supplementary information and  
 310 presented in figures 2 to 5.

311 **3.1 U-Pb zircon geochronology**

312 A total of 98 zircons from 7 volcanic ash beds were analyzed. Zircon U and Pb data are  
 313 presented in the supplementary information and interpreted U-Pb dates are illustrated in Fig. 2.  
 314 For each volcanic ash bed, the U-Pb weighted mean date is interpreted on the following basis: i)  
 315 not rejecting any analyses that are concordant, ii) the youngest cluster of interpreted concordant  
 316 zircons consists of  $\geq 3$  analyses and iii) assuming that all Pb-loss is effectively removed by the  
 317 chemical abrasion procedure.

318 Only in one sample (POT 66T) do we reject one younger, concordant analysis, as it is  
 319 younger than the statistically significant, slightly older age plateau of 12 analyses (Fig. 2). Zircon  
 320 from ash bed POT 66T has the greatest amount of radiogenic Pb relative to other samples in this  
 321 study (Table S1, supplementary information). Analyses that are older than the youngest,  
 322 statistically valid, date plateau are considered detrital or due to inherited or antecrystic cores.  
 323 Applying this strategy, volcanic ash beds LAX8T, LAX10T, POT66T, POT67T and POT68T  
 324 have statistically significant  $^{206}\text{Pb}/^{238}\text{U}$  weighted mean ages of  $252.07 \pm 0.13/0.15/0.31$  Ma  
 325 (Mean Square Weighted Deviation (MSWD) = 1.3,  $n = 5$ ),  $251.822 \pm 0.060/0.089/0.28$  Ma  
 326 (MSWD = 1.9,  $n = 6$ ),  $251.589 \pm 0.052/0.083/0.28$  Ma (MSWD = 1.67,  $n = 12$ ),  $251.668 \pm$   
 327  $0.079/0.10/0.29$  Ma (MSWD = 1.99,  $n = 9$ ) and  $251.64 \pm 0.13/0.15/0.31$  Ma (MSWD = 1.5,  $n =$   
 328 12), respectively (Fig. 2).

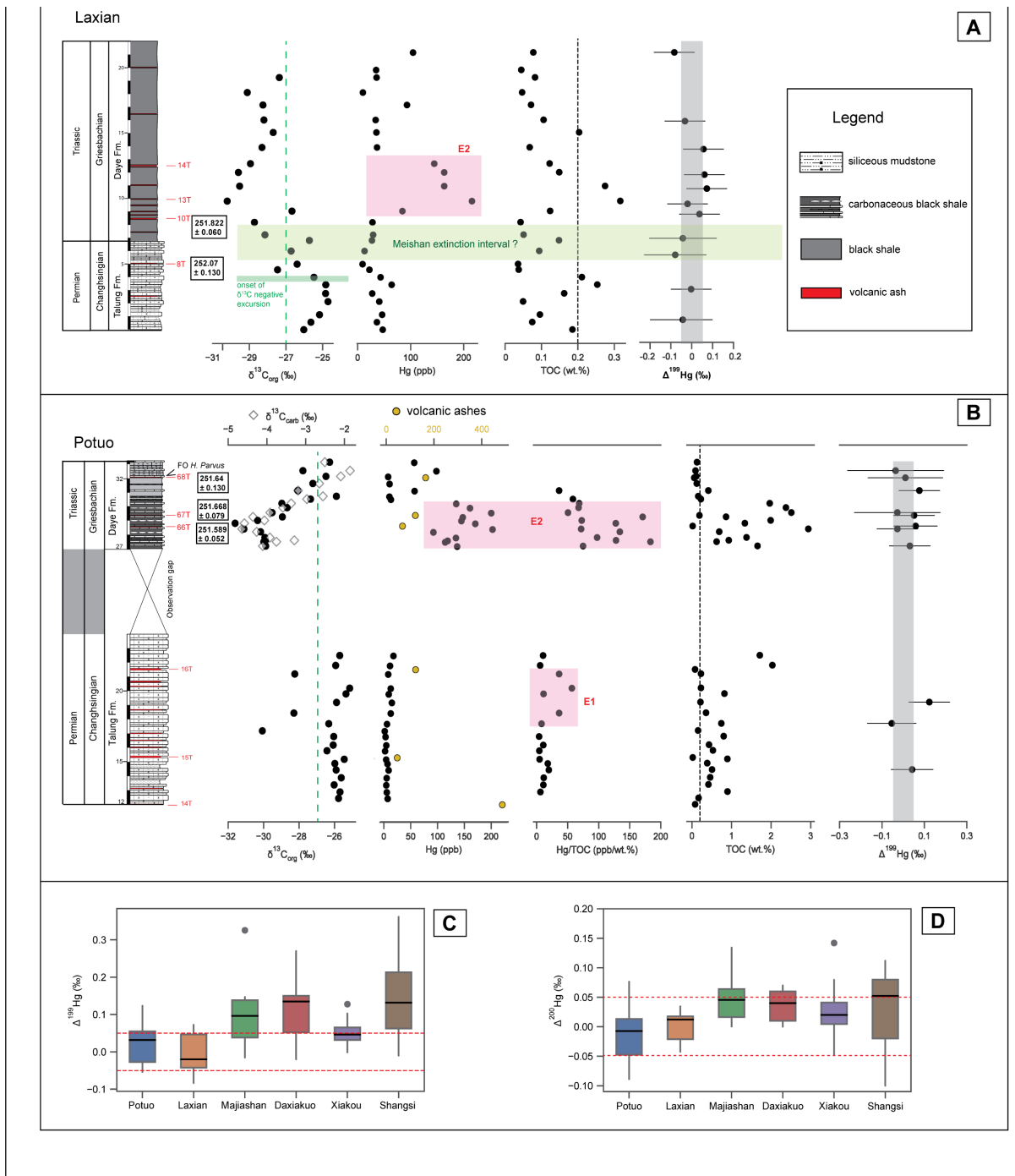


329

330 Figure 2: Single-grain zircon analyses and  $^{206}\text{Pb}/^{238}\text{U}$  weighted mean dates for volcanic ash beds  
 331 from Potuo and Laxian. Bars represent single grain zircon U-Pb dates and their uncertainty.  
 332 Transparent bars are rejected for interpretation (Pb-loss, inheritance, antecrystic).

333 3.2 TOC contents and Hg concentrations

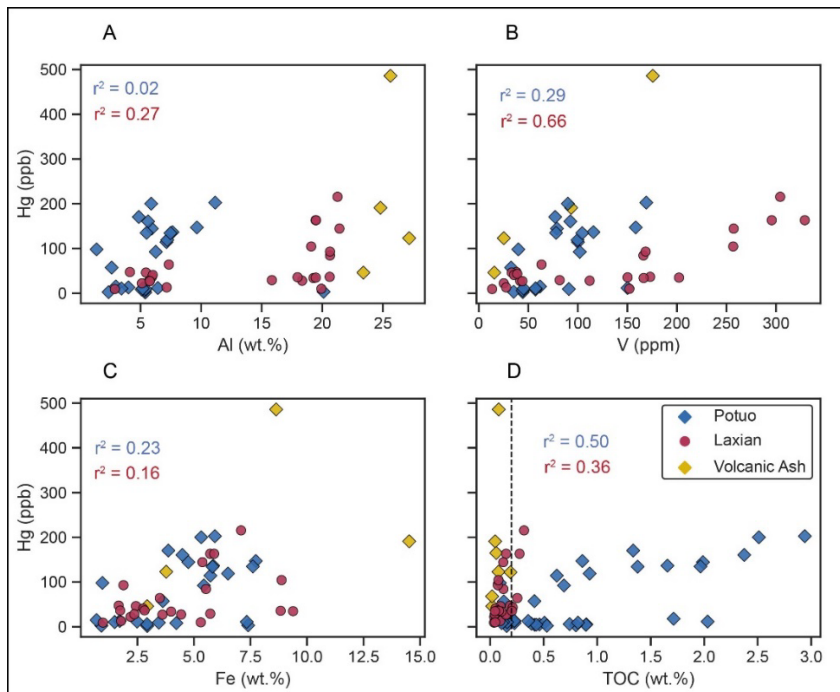
334 TOC content is stratigraphically variable and generally low for Laxian relative to Potuo  
 335 with a range between < 0.1 – 0.3 wt.% and 0.1 – 2.9 wt.% respectively (Fig. 3). TOC generally  
 336 shows moderate correlation for Laxian ( $r^2 = 0.36$ ) and Potuo ( $r^2 = 0.50$ ) (Fig. 4). Only 3 samples  
 337 for Laxian have TOC content above 0.2 wt.%, a suggested threshold for robust Hg/TOC  
 338 normalization (Grasby et al., 2019). In contrast, only 6 out of 38 samples for Potuo have TOC  
 339 values < 0.2 wt.%. Therefore, Hg data for Laxian are not normalized to TOC.



341 Figure 3. Carbon isotope values, Hg concentrations, Hg/TOC ratios, TOC contents and  $\Delta^{199}\text{Hg}$   
 342 Hg values from a) Laxian, b) Potuo. The gap between the Talung and Daye formations in the Potuo  
 343 stratigraphic log is an observation gap due to coverage by alluvium (Bagherpour et al., 2020).  
 344 Black dashed lines represent the 0.2 wt.% TOC limit for Hg/TOC normalization (Grasby et al.,  
 345 2019) and green dashed lines represent background  $\delta^{13}\text{C}_{\text{org}}$  values (-27 ‰). Box and whisker  
 346 plots of c)  $\Delta^{199}\text{Hg}$  values and d)  $\Delta^{200}\text{Hg}$  values for Potuo and Laxian compared to those  
 347 previously documented for other deep-water marine sections in South China. Grey shaded  
 348 rectangle (in a, b) and red dashed lines (in c, d) represent the interval of no measurable Hg  
 349 isotope mass independent fractionation (MIF,  $0 \pm 0.05$  ‰). Data sources are as follows:  
 350 Majiashan - Wang et al.(2019a), Daxiakou - Wang et al. (2018), Xiakou - J. Shen et al. (2019),  
 351 Shangsi - J. Shen et al. (2021).

352 Hg concentrations of samples from the Talung Fm. in Potuo range between 2 ppb and 18  
 353 ppb and are generally lower than for Laxian, which range between 9 ppb and 64 ppb. The main  
 354 feature of the latest Permian Hg record for Potuo is a minor Hg/TOC excursion (referred to as E1  
 355 here) with a peak Hg/TOC value of 70 ppb/wt.%. In the Daye Fm., a significant Hg  
 356 concentration increase (here labelled as E2) is recorded in the lower part of the successions at  
 357 both sections. This Hg excursion is simultaneously expressed by the Hg and Hg/TOC records for  
 358 Potuo (Fig. 3). Peak Hg concentrations within E2 Hg anomaly (Laxian = 251 ppb, Potuo = 203  
 359 ppb) are higher than the mean so far reported (62 ppb) for sedimentary rocks (Grasby et al.,  
 360 2019).

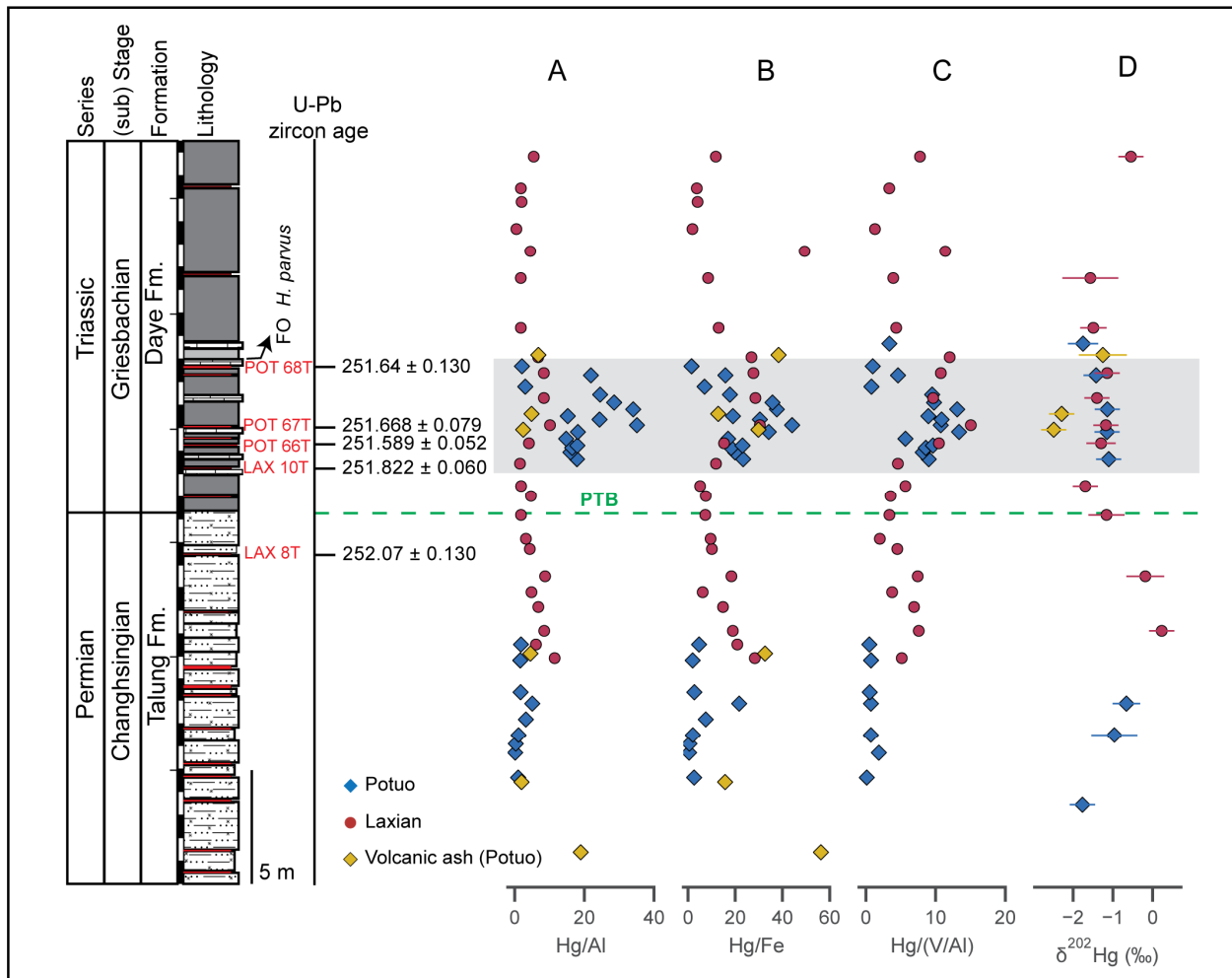
361 Volcanic ashes from the Talung Fm. at Potuo have Hg concentrations that are at least one  
 362 order of magnitude higher than for interbedded siliceous mudstones. This difference does not  
 363 hold in the Daye Fm., where Hg concentration values range between 68 ppb and 165 ppb for  
 364 volcanic ashes and between 84 ppb and 203 for interbedded rocks within the E2 Hg anomaly  
 365 interval (Fig. 3b).



367 Figure 4. Scatter plot showing the relationship between Hg and a) Al, b) V, c) Fe and d) TOC in  
 368 the Pingtang syncline sections. Black dashed line represents 0.2 wt.% TOC limit (Grasby et al.,  
 369 2019). Volcanic ash samples are not included in the calculation of the correlation coefficient  
 370 squared ( $r^2$ ).

371 3.3 Mercury isotopes

372 Mass dependent fractionation of Hg isotopes ( $\delta^{202}\text{Hg}$ ) shows near-zero to negative values  
 373 for both sections throughout the studied interval (range:  $+0.23 \pm 0.32 \text{ ‰}$  to  $-1.75 \pm 0.32 \text{ ‰}$ ;  
 374 mean =  $-1.13 \pm 1.02 \text{ ‰}$ ), except for 2 volcanic ash samples from Potuo with more negative  
 375 values (Fig. 5, POT66T:  $-2.49 \pm 0.32 \text{ ‰}$  and POT67T:  $-2.29 \pm 0.32 \text{ ‰}$ ).



376  
 377 Figure 5. Composite plot of Hg/element ratios and Hg isotope mass dependent fractionation  
 378 values for Potuo and Laxian. a) Hg/Al, b) Hg/Fe, c) Hg/(V/Al), d)  $\delta^{202}\text{Hg}$ . Symbols of  
 379 lithological log are identical to those of Fig. 3.

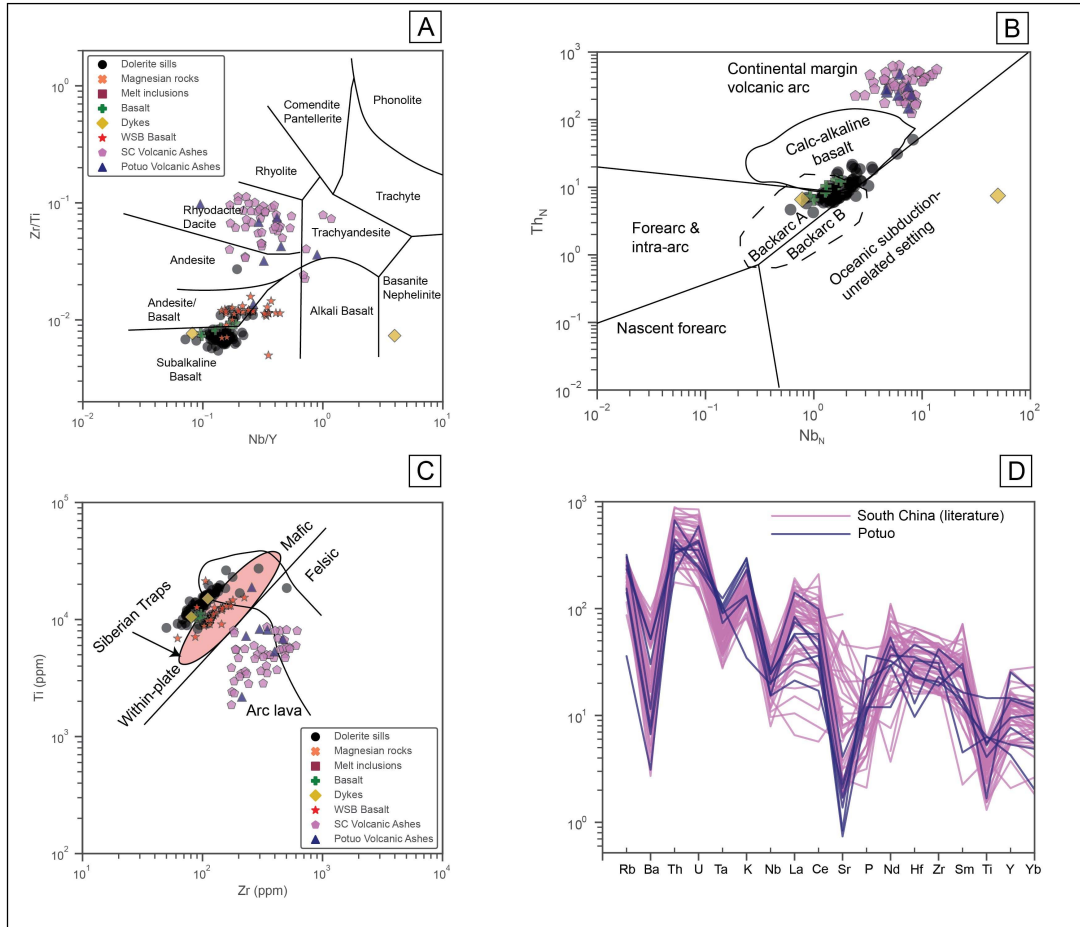
380 The range and mean  $\delta^{202}\text{Hg}$  values are comparable with  $\delta^{202}\text{Hg}$  values measured from  
 381 bulk volcanic Hg emissions (Zambardi et al., 2009; Sun et al., 2016), and lighter  $\delta^{202}\text{Hg}$  values  
 382 recorded for volcanic ashes are congruent with similar observations for particulate volcanic Hg  
 383 (Zambardi et al., 2009). Hg isotope MIF ( $\Delta^{199}\text{Hg}$  and  $\Delta^{200}\text{Hg}$ ) values for both sections are near-  
 384 zero throughout the studied interval (i.e.,  $0.1 \text{ ‰} > z > -0.1 \text{ ‰}$ , where  $z$  = sample Hg MIF value),

385 except for sample POT 59, which has a  $\Delta^{199}\text{Hg}$  value of  $0.12 \pm 0.11$  ‰. Mean ( $\pm 2\sigma$ )  $\Delta^{199}\text{Hg}$   
 386 values are  $0.02 \pm 0.11$  ‰ and  $-0.01 \pm 0.11$  ‰ for Potuo and Laxian respectively. For Potuo, the  
 387 mean  $\Delta^{200}\text{Hg}$  value is  $-0.01 \pm 0.10$  ‰ and for Laxian, it is  $0.00 \pm 0.05$  ‰. Hence, the Pingtang  
 388 syncline sections record no measurable mass independent fractionation of Hg isotopes, in  
 389 contrast to Hg isotope records for deep-water marine sections outside the Nanpanjiang Basin in  
 390 South China (Fig. 3c).

### 391 3.4 Major and Trace Elements

392  $\text{Al}_2\text{O}_3$  concentrations for both sections show similar patterns, having lower values in the  
 393 Talung Fm. (with a range of 2 to 4 wt.%, except for 1 Potuo sample) relative to the Daye Fm. For  
 394 Laxian,  $\text{Al}_2\text{O}_3$  values in the Daye Fm. are 3× higher (range: 15 – 22 wt.%) than those of the  
 395 Talung Fm.  $\text{Fe}_2\text{O}_3$  concentrations show a similar trend to  $\text{Al}_2\text{O}_3$ , with lower values in the Talung  
 396 Fm. (1 to 5 wt.%) relative to the Daye Fm. for both localities. However, unlike  $\text{Al}_2\text{O}_3$ , values in  
 397 the Daye Fm. for both localities are identical (between 2 and 9 wt.%). Al and Fe (proxied by  
 398  $\text{Al}_2\text{O}_3$  and  $\text{Fe}_2\text{O}_3$ ) show little to no correlation with Hg for both Potuo (Al:  $r^2=0.21$ , Fe:  $r^2=0.29$ )  
 399 and Laxian (Al:  $r^2=0.27$ , Fe:  $r^2=0.16$ ). V contents are higher in the Daye Fm. relative to the  
 400 Talung Fm. in both localities and shows stronger correlation with Hg for Laxian ( $r^2=0.66$ ) than  
 401 for Potuo ( $r^2=0.38$ ) (Fig. 4).

402 Volcanic ash samples have high LOI (loss on ignition) values between 9 to 14 wt.%,  
 403 consistent with results from contemporaneous ash layers in South China (He et al., 2014). The  
 404 ash samples have LOI-corrected mean ( $\pm 1\sigma$ ) concentrations of  $58 \pm 5$  wt.%,  $25 \pm 2$  wt.% and  $5$   
 405  $\pm 3$  wt.% for  $\text{SiO}_2$ ,  $\text{Al}_2\text{O}_3$  and total alkali ( $\text{Na}_2\text{O}+\text{K}_2\text{O}$ ) respectively (Table S2, supplementary  
 406 information). To mitigate the chemical effects of secondary alteration of the volcanic ashes, only  
 407 immobile elements (such as Th, Nb, Ta, Zr, Hf, Ti, Y), known to be unaffected by post-  
 408 depositional alteration (Portnyagin et al., 2020), are utilized for subsequent chemical  
 409 classification and tectonic interpretation (Fig. 6). The ashes mainly plot within the fields of  
 410 rhyodacite/dacite, andesite and trachyandesite on the Nb/Y vs. Zr/Ti diagram (Winchester and  
 411 Floyd, 1977), separate from STLIP volcanic rocks, except for 1 sample: POT 14T (Fig. 6a).  
 412 Incompatible trace elements normalized against primitive mantle values (Sun and McDonough,  
 413 1989) show that the volcanic ashes are characterized by pronounced negative Nb, Ta and Ti  
 414 anomalies (Fig. 6d), similar to the trace element pattern for volcanic ashes from other localities  
 415 in South China (He et al., 2014; Yang et al., 2012).



416  
 417 Figure 6: Major and trace element geochemistry results for volcanic ash samples from the  
 418 Pingtang syncline. a)  $Zr/Ti$  vs  $Nb/Y$  classification diagram (Winchester & Floyd, 1977) for  
 419 volcanic ashes from South China plotted along with volcanic rocks from the Siberian Traps  
 420 Large Igneous Province (STLIP) b) N-MORB-normalized Th vs. Nb discriminant plot, with  
 421 tectonic setting interpretation after Saccani et al. (2015, 2018) for volcanic ashes from South  
 422 China, together with data from dolerite sills, dykes and basalts from the STLIP (Tunguska Basin)  
 423 plotted for comparison. N-MORB: normal-type mid-oceanic ridge basalt. c) Ti vs Zr  
 424 classification diagram after Pearce (1982). The field illustrating typical Siberian Traps volcanic  
 425 rock compositions is after He et al. (2014). d) Primitive mantle-normalized spider diagram for  
 426 Changhsingian and Griesbachian volcanic ashes from Potuo and other localities (Meishan,  
 427 Chaotian, Jianshi, Rencunping, Shangsi and Dongpan) in South China. Data for South China  
 428 localities other than Potuo are from He et al. (2014), Song et al. (2022) and Wang et al. (2019b).  
 429 Normalization values for N-MORB and primitive mantle are from Sun & McDonough (1989).  
 430 Data for volcanic rocks from the STLIP are from several sources as follows: basalt flows,  
 431 dolerite sills, dykes: Sibik et al. (2015); Callegaro et al. (2021); magnesian rocks, melt  
 432 inclusions: Sobolev et al. (2009); West Siberia Basin (WSB) basalts: Reichow et al. (2005).  
 433 WSB: West Siberia Basin, SC: South China.

434 **4 Discussion**

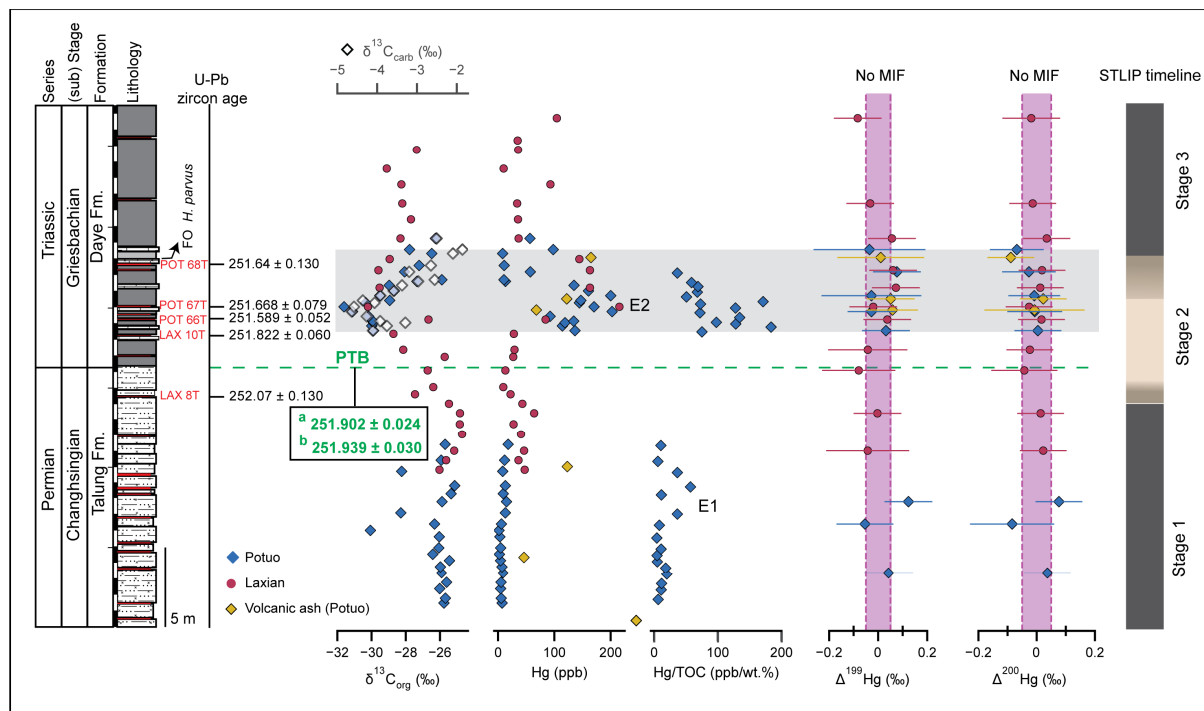
## 435 4.1 Sedimentary hosts of Hg and interpretation of the Hg anomalies

436 Hg enrichment in sediments may reflect enhanced Hg sequestration related to increased  
437 abundance of its sedimentary host phase(s) or enhanced Hg input fluxes during sediment  
438 deposition (Grasby et al., 2019; J. Shen et al., 2020). Due to the high affinity of Hg for organic  
439 matter (OM), Hg concentration is usually normalized to TOC content to account for any OM  
440 increases that could have preferentially enhanced Hg sequestration in sediments (e.g., Sanei et  
441 al., 2012; Grasby et al., 2017, 2019). However, in samples with low OM content (< 0.2 wt.%  
442 TOC), the Hg/TOC ratio is deemed unreliable as the Hg/TOC values become exaggerated,  
443 producing false Hg/TOC peaks (Grasby et al., 2019; but see Yager et al., 2021). In addition to  
444 TOC variations, Hg sequestration in sedimentary rocks can be influenced by other sedimentary  
445 host phases such as clay minerals, iron oxides and sulfides (Charbonnier et al., 2017; J. Shen et  
446 al., 2020).

447 Based on cross plots of Hg vs. Al, Fe and V content for both sections, Hg is best  
448 correlated to TOC and V compared to Al and Fe (Fig. 4). This potentially indicates that Hg  
449 sequestration in the studied sites was partially controlled by marine redox conditions, proxied by  
450 V (Hammer et al., 2019) and may explain the more efficient sequestration of Hg in the black  
451 shales of the Daye Formation relative to the siliceous mudstones of the Talung Formation.  
452 Nevertheless, plots of Hg/Al, Hg/Fe and Hg/(V/Al) ratios for both localities, including Hg/TOC  
453 for Potuo (Fig. 3; Fig 5) show similar trends of peak Hg contents in the lower part of the  
454 Griesbachian record, suggesting that the Hg anomaly in this interval cannot be explained by  
455 redox variations, TOC variability or clay mineral inputs alone. Furthermore, lithological changes  
456 are unlikely to control the Hg concentration spike as increases in Hg concentration do not  
457 coincide with the change in lithology in neither of the two sections. Moreover, relatively high  
458 and low Hg concentrations alike are measured for the Talung and Daye formations where Hg and  
459 Hg/TOC anomalies are recorded (Fig. 3; Fig. 7). These observations suggest that a dominant host  
460 of Hg in the studied sections is difficult to pinpoint and that instead, Hg may be distributed  
461 between different hosts.

462 Hg isotopes are used to trace the source(s) and depositional pathway(s) of Hg to natural  
463 environments, as Hg isotope mass-dependent fractionation ( $\delta^{202}\text{Hg}$ ) and mass-independent  
464 fractionation (MIF,  $\Delta^{199}\text{Hg}$  and  $\Delta^{200}\text{Hg}$ ) compositions vary across Earth surface reservoirs and  
465 transport mechanisms (Bergquist & Blum, 2007; Blum et al., 2014; Fu et al., 2021). Here, we  
466 focus on Hg isotope MIF, as this occurs via fewer processes compared to MDF (Blum et al.,  
467 2014), and has been demonstrated to be unaffected by high-temperature, high-pressure alteration  
468 of rocks (Chen et al., 2022). Furthermore, volcanic  $\delta^{202}\text{Hg}$  values overlap with those of terrestrial  
469 runoff and atmospheric  $\text{Hg}^{\text{II}}$  deposition (Yager et al., 2021), making them less diagnostic than Hg  
470 isotope MIF values.  $\Delta^{199}\text{Hg}$  is commonly used to interpret the sources and pathways of Hg  
471 deposition (Thibodeau & Bergquist, 2017; Yager et al., 2021) and recently,  $\Delta^{200}\text{Hg}$  has been  
472 proposed as a complementary tracer of Hg sources to land and oceans (Jiskra et al., 2021). This  
473 is because even number-Hg isotope MIF (e.g.,  $\Delta^{200}\text{Hg}$ ) only occurs via upper atmospheric  
474 oxidation-reduction pathways and thus, Hg transformations near Earth's surface yield no  
475 measurable even number-Hg isotope MIF (Chen et al., 2012; Fu et al., 2021). Hg derived from  
476 direct volcanic emission is thought to have no measurable MIF (i.e.,  $\Delta^{199}\text{Hg}$ ,  $\Delta^{200}\text{Hg} = \sim 0 \text{ ‰}$ )  
477 and  $\delta^{202}\text{Hg}$  values between -2 and 0 ‰ (Thibodeau & Bergquist, 2017; Zambardi et al., 2009).

478 The near zero and invariant  $\Delta^{199}\text{Hg}$  and  $\Delta^{200}\text{Hg}$  values throughout our studied interval (Fig. 7)  
 479 are thus interpreted to reflect a dominant atmospheric volcanic Hg source to the Nanpanjiang  
 480 Basin. Consequently, the Hg and Hg/TOC anomalies recorded for both localities reflect pulses of  
 481 elevated atmospheric volcanic Hg input to these deep-water marine depositional sites.  
 482



483  
 484 Figure 7: Composite  $\delta^{13}\text{C}$ , Hg concentration and  $\Delta^{199}\text{Hg}$ ,  $\Delta^{200}\text{Hg}$  MIF (mass independent  
 485 fractionation) records from the Potuo and Laxian sections.  $\delta^{13}\text{C}$  values are from Bagherpour et  
 486 al. (2020). The horizontal gray band marks the interval of Hg concentration spike and nadir of  
 487 the negative  $\delta^{13}\text{C}$  excursion and the vertical pink bands depict near-zero Hg isotope MIF ( $0 \pm$   
 488  $0.05$  ‰, Thibodeau et al., 2016). The dashed green line represents the conformable Talung-Daye  
 489 formational boundary and the PTB. The Siberian Traps magmatism timeline is after Burgess et  
 490 al. (2017) and the color gradient between the stages depicts the uncertainty in the timing of the  
 491 transition between different stages. The PTB on the composite log is defined from the Laxian  
 492 section as this interval at Potuo is covered by recent alluvial deposits (Bagherpour et al., 2020).  
 493 U-Pb zircon ages for the PTB (in green) are from (a) Burgess et al. (2014) and (b) Baresel et al.  
 494 (2017b). FO – first occurrence.

#### 495 4.2 U-Pb zircon age constraints on the Hg anomaly and C isotope excursion

496 Although previous works (Grasby et al., 2017; J. Shen et al., 2019; Sial et al., 2020)  
 497 suggested a coeval global occurrence of Hg anomalies around the PTBME, the majority of  
 498 sections with defined Hg anomalies around the Permian-Triassic transition lack high-resolution,  
 499 high-precision geochronology. Our study attempts to specifically bracket the age of a well-  
 500 defined Hg anomaly in the Early Triassic via dating of under and overlying ash beds in expanded  
 501 deep-water marine records. The new U-Pb zircon ages from the Pingtang syncline span the onset  
 502 of the latest Permian negative  $\delta^{13}\text{C}$  excursion, ca.  $252.07 \pm 0.130$  Ma and brackets a  
 503 Griesbachian Hg anomaly. The two ash layers analyzed from Laxian straddle the PTB and the U-  
 504 Pb ages are consistent with the stratigraphy, yielding U-Pb weighted mean ages of  $252.07 \pm 0.13$

505 Ma (LAX8T, latest Permian) and  $251.822 \pm 0.060$  Ma (LAX10T, Griesbachian) respectively.  
506 These U-Pb zircon ages overlap, within analytical error, with the ages of Bed 25 ( $251.941 \pm$   
507  $0.037$  Ma) and Bed 28 ( $251.880 \pm 0.031$  Ma) of the very condensed Meishan Global Stratotype  
508 Section and Point (GSSP) (Burgess et al., 2014). Thus, the interval between LAX8T and  
509 LAX10T includes the PTBME interval at Meishan and also agrees with previous suggestions  
510 that the conformable lithological boundary between the Talung/Dalong and Daye/Ziyun  
511 formations accurately delineates the PTB in deep-water marine successions in the Nanpanjiang  
512 Basin (Bagherpour et al., 2020; Baresel et al., 2017b). The Changhsingian Hg/TOC anomaly  
513 (E1), recorded from Potuo, is older than LAX 8T and as such, predates the mass extinction  
514 interval.

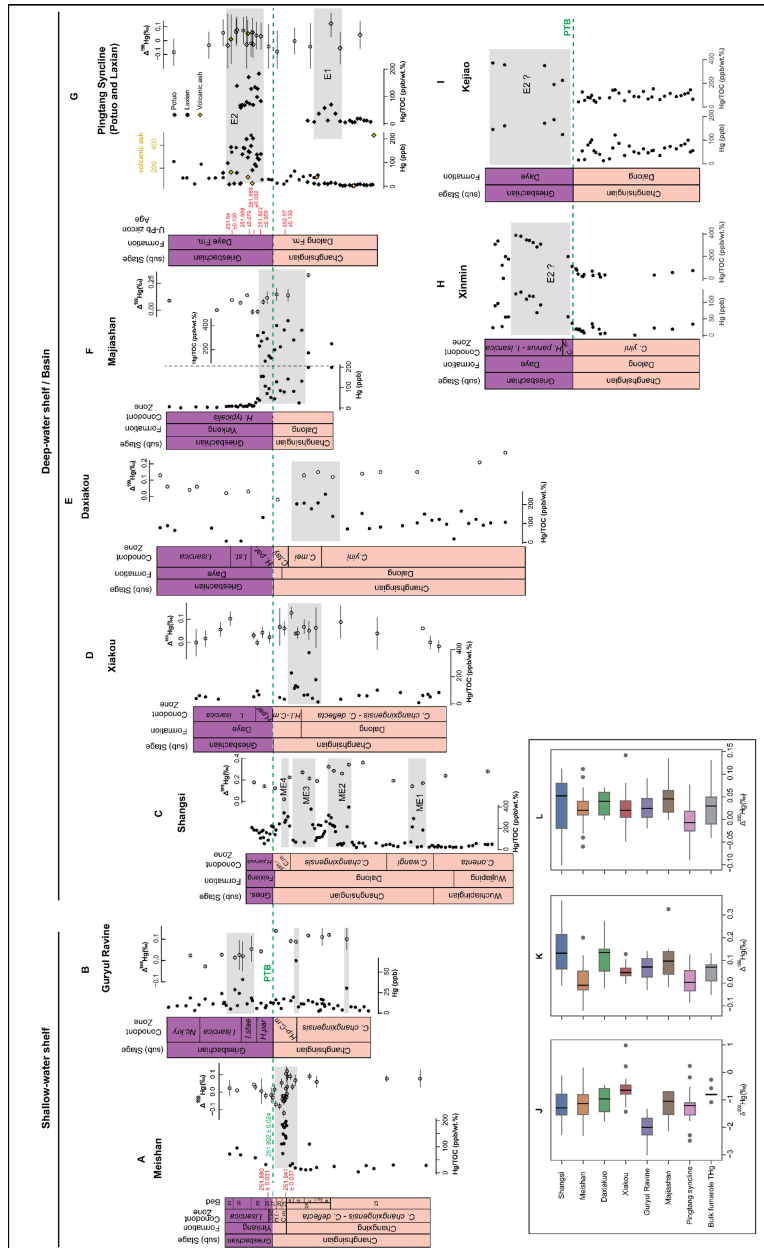
515 The overlap between the  $^{206}\text{Pb}/^{238}\text{U}$  weighted mean ages of ash beds POT 66T, 67T and  
516 68T suggests the occurrence of several successive volcanic eruptions (within the time covered by  
517 these volcanic ash layers) at intervals shorter than the resolving power of our ID-TIMS U-Pb  
518 geochronology at the given quality of zircon available for this study. Nevertheless, as these  
519 volcanic ash layers from Potuo straddle both the Hg anomaly recorded in the Daye Fm., as well  
520 as the coeval nadir of the negative  $\delta^{13}\text{C}$  excursion (Fig. 7), the age of both the Hg anomaly (E2)  
521 and peak C-cycle perturbation during the Permian-Triassic transition can be determined. The  
522 youngest age for both the peak of the E2 Hg anomaly and the nadir of the  $\delta^{13}\text{C}$  excursion is  
523  $251.589 \pm 0.052$  Ma (POT66T, Fig. 7), while the oldest age estimate is  $251.668 \pm 0.079$  Ma  
524 (POT67T). These two ages are identical within the analytical (X) uncertainty, precluding an  
525 estimation of the duration of the Hg anomaly. Despite these uncertainties, we can establish with  
526 confidence that the post-PTB Hg anomaly peak observed in Potuo is ca. 300 kyr younger (largely  
527 outside of analytical uncertainty) than the Meishan PTBME interval (Burgess et al., 2014;  
528 Burgess and Bowring, 2015), as well as the extinction horizon in Penglaitan ( $251.939 \pm 0.031$   
529 Ma; S. Shen et al., 2019).

#### 530 4.2.1 Hg anomalies as a PTBME correlation tool

531 A negative  $\delta^{13}\text{C}$  excursion at the Permian-Triassic transition together with a Hg anomaly  
532 are common features of many PTB-straddling sedimentary successions (Fig. 8; Fig. 9). As such,  
533 the peak of the Hg anomaly and/or the nadir of the negative  $\delta^{13}\text{C}$  excursion associated with the  
534 PTB are often used for delineating and correlating the PTBME extinction interval (e.g., Grasby  
535 et al., 2017; Sial et al. 2020; J. Shen et al. 2019, 2023). Although some sedimentary successions,  
536 especially in high latitudes, show Hg excursions coincident with both the negative  $\delta^{13}\text{C}$   
537 excursion and mass extinction (e.g., Sanei et al., 2012; Grasby et al., 2013), it is apparent that Hg  
538 excursions in several other successions straddling the PTB vary in expression, timing, and  
539 vertical stratigraphic extent (Fig. 8; Fig. 9). Hence, questioning the reliability of these Hg  
540 anomalies for positioning the PTBME and the use of Hg anomalies as a stratigraphic correlation  
541 tool.

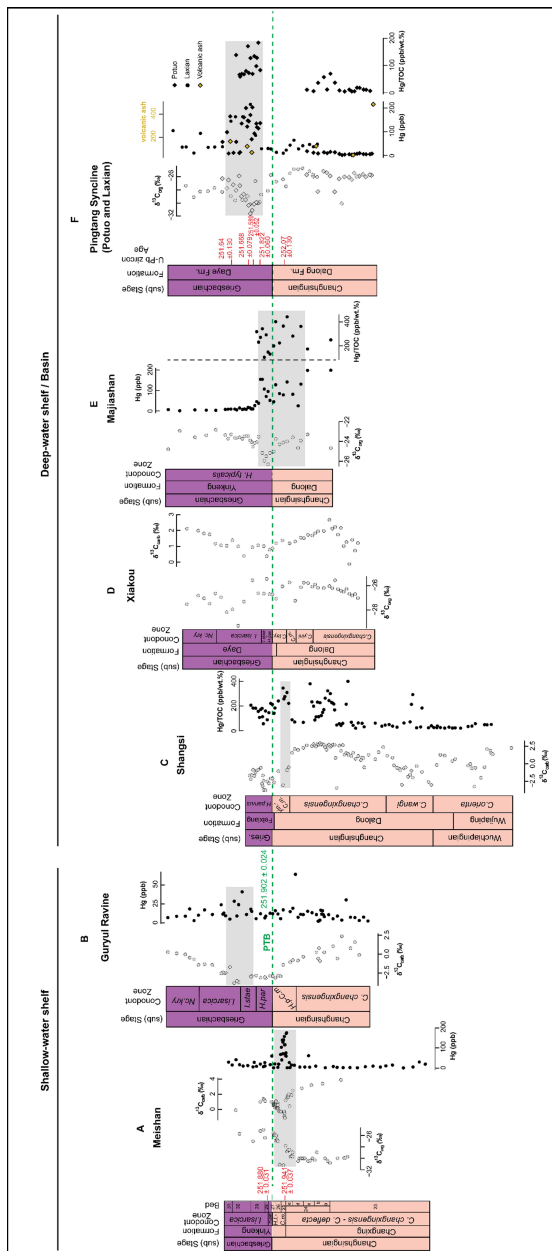
542 In the case of the Pingtang syncline record, neither Hg excursion (E1 nor E2) temporally  
543 corresponds to the extinction interval as calibrated in the Meishan GSSP (Fig. 3; Fig. 7). Also, no  
544 Hg anomaly is recorded at the PTBME extinction interval in Laxian (i.e., between LAX 8T and  
545 10T, Fig. 3), although the equivalent stratigraphical interval in Potuo is a visibility gap  
546 (Bagherpour et al., 2020). As such, the presence of a Hg anomaly there cannot be formally  
547 excluded. Nevertheless, our U-Pb zircon ages show that both the nadir of the PTB negative  $\delta^{13}\text{C}$   
548 excursion and the peak of the stratigraphically nearest Hg anomaly to the PTB (E2) are of  
549 Griesbachian age (between  $251.589 \pm 0.052$  Ma and  $251.668 \pm 0.079$  Ma). Thus, these data

550 provide evidence that although Hg anomalies may coincide with the nadir of the PTB negative  
 551  $\delta^{13}\text{C}$  excursion (Fig. 9), this correspondence cannot be reliably used as a stratigraphic marker for  
 552 the PTBME in a single section or between different sections (and/or different basins). Similar  
 553 conclusions were reached for the end-Triassic extinction (ETE) event by Yager et al. (2021),  
 554 who documented “mismatches in timing” between Triassic-Jurassic boundary Hg anomalies and  
 555 Central Atlantic Magmatic Province (CAMP) magmatism, which is purported to have triggered  
 556 the ETE event. Hence, positioning the PTB extinction event by means of and/or correlation  
 557 based on Hg or C isotope chemostratigraphy should be treated with extreme caution.



558 Figure 8: Compilation of mercury (Hg) concentration and isotope ( $\Delta^{199}\text{Hg}$ ) records for marine  
 559 depositional environments in the Tethys region: South China and northern India (A – I). Hg/TOC  
 560 ratios are shown only for localities and stratigraphic intervals where TOC content is > 0.2 wt.%.  
 561 a) Meishan. U-Pb zircon ages are from Burgess et al. (2014), b) Guryul Ravine, northern India,  
 562

563 c) Shangsi, d) Xiakou, e) Daxiakou, f) Chaohu, g) Pingtang syncline (composite of the Potuo and  
 564 Laxian sections), h) Xinmin, i) Kejiao. The different profiles are correlated using the Permian-  
 565 Triassic boundary as placed by the authors of the original data sources. Box and whisker plots of  
 566 j)  $\delta^{202}\text{Hg}$ , k)  $\Delta^{199}\text{Hg}$  and l)  $\Delta^{200}\text{Hg}$  values for the above-mentioned localities compared with  
 567 measurements for bulk fumarole total Hg (THg, Sun et al., 2016). Data sources for  
 568 stratigraphical log and Hg data are as follows: Meishan: Grasby et al. (2017) and J. Shen et al.  
 569 (2019); Guryul Ravine and Majiashan: Wang et al. (2019a); Shangsi: J. Shen et al. (2021);  
 570 Xiakou, Xinmin, Kejiao: J. Shen et al. (2019); Daxiakou: Wang et al. (2018); Pingtang syncline  
 571 (Potuo, Laxian): this study. Abbreviations: Gries.: Griesbachian; *H.l.*: *Hindeodus latidentatus*;  
 572 *C.m.*: *Clarkina meishanensis*; *H.par.*: *Hindeodus parvus*; *H.p.*: *Hindeodus praeparvus*; *I.st.*:  
 573 *Isarcicella staeschei*; *Nc.kry.*: *Neoclarkina krystyni*; *yin.*: *Clarkina yini*; *C.tay.*: *Clarkina*  
 574 *taylorae*.



576 Figure 9. Carbon (organic and carbonate) isotope, mercury (Hg) concentration and Hg/TOC  
577 records for Permian-Triassic sections in the PaleoTethys (South China) and NeoTethys (northern  
578 India) regions. a) Meishan. b) Guryul ravine, northern India. c) Shangsi. d) Xiakou. e)  
579 Majiashan. f) Pingtang syncline (composite of Potuo and Laxian sections). All abbreviations are  
580 as for Figure 8. Data sources are as follows: Meishan: Carbon (C) isotope data is from Cao et al.  
581 (2002), Xiakou: C isotope and stratigraphical data are from G.J. Zhang et al (2021). U-Pb zircon  
582 age for the Permian-Triassic boundary (in green) is from Burgess et al. (2014). Apart from the  
583 Xiakou section, all other stratigraphic data sources are as for Figure 8.

584 4.3 Does the E2 Hg anomaly of Griesbachian age coincide with a 2<sup>nd</sup> extinction event?

585 The onset of the Griesbachian Hg anomaly as recorded from the Laxian section (Fig. 3)  
586 postdates LAX 10T, which is dated at  $251.822 \pm 0.060$  Ma. This age coincides, within analytical  
587 uncertainty, with that determined for Bed 28 at the Meishan GSSP ( $251.880 \pm 0.031$  Ma;  
588 Burgess et al., 2014). Because a second step of the PTB mass extinction has been postulated to  
589 have occurred within Bed 28 in Meishan (Song et al., 2013), it is pertinent to consider whether  
590 the E2 Hg anomaly is associated with this proposed second extinction step.

591 Conodont biozones around the PTB are usually interval zones (IZs), with the base of each  
592 IZ being defined by the first occurrence (FO) of an index species and the top defined by the base  
593 of the next overlying IZ. However, this biostratigraphical correlation technique often leads to  
594 diachronous correlations because the relative stratigraphic order of FOs of index species is not  
595 constant across space, as demonstrated by Brosse et al. (2016) for conodonts around the PTB in  
596 South China. Reasons for diachronous IZs include ecological control over the distribution of  
597 species in time and space, sampling effort, selective preservation, and hiatuses in the sedimentary  
598 record (Guex, 1991; Holland & Patzkowsky, 2015; Leu et al., 2022). However, following this  
599 approach, the “legal” base Triassic was defined by the FO of *Hindeodus parvus* in the very  
600 condensed Meishan section (Yin et al., 2001).

601 Song et al. (2013) compiled FOs and LOs (last local occurrences) for conodonts and  
602 benthic taxa from seven South Chinese PTB sections (including Meishan and Shangsi), which  
603 led the authors to propose two extinction steps. The main and older event was placed at the base  
604 of the *C. meishanensis* IZ, the antepenultimate IZ below the FO of *H. parvus*. The proposed  
605 second extinction step, of lesser magnitude, was found at the base of the *I. isarcica* IZ, which is  
606 the third Triassic IZ above the spatially variable FO of *H. parvus*. However, a recent thorough  
607 re-investigation of Late Permian conodont IZs in the more expanded Shangsi section (Yuan et  
608 al., 2019) led to a revision of the basal Triassic into the *C. meishanensis* IZ. This new placement  
609 of the base of the Triassic (Yuan et al. 2019; written comm. 2022) in the *C. meishanensis* IZ in  
610 Shangsi and Meishan has the intrinsic benefit of coinciding with both the main extinction event  
611 and the lithostratigraphic boundary between Permian and Triassic rock units, which is marked by  
612 a hiatus in outer shelves and shallower depositional settings in South China and elsewhere  
613 (Bagherpour et al., 2017; Yin et al., 2014). Close examination of the raw biostratigraphic data  
614 (Table S2 of Song et al. 2013) from which a second extinction step was postulated shows no  
615 consistent extinction in the relative timing of the different species across the data set. Extinction  
616 of a given clade occurs in a single section, or pair of sections at the very best, thus undermining  
617 arguments in favor of a second extinction event of global significance. For instance, only the  
618 condensed Meishan section displays an apparent second step for benthic foraminifers and  
619 bivalves. In Shangsi, no second extinction emerges for any benthic clade around the base of *the*  
620 *I. isarcica* IZ.

621 Furthermore, the compositing of local extinctions patterns (Song et al. 2013) relies on the  
622 implicit assumption of synchronous conodont IZs. However, as the seven sections of this data set  
623 cover a very broad range of water depths, ranging from lagoon-shoals to lower slope-basin  
624 (Table S1 of Song et al. 2013,), the assumption of synchronous conodont IZs becomes untenable.  
625 It is also at variance with the fact that the respective bathymetric distribution of segminate and  
626 segminiplanate conodonts, both involved as index species of IZs, is known to be spatially  
627 controlled by temperature – i.e., depth of water masses (Joachimski et al., 2012; Leu et al.,  
628 2019). Moreover, the general development of a hiatus spanning approximately the entire *C.*  
629 *meishanensis* IZ in shallower depositional settings as clearly established by Yin et al. (2014)  
630 automatically excludes any synchronicity of the neighboring IZ when comparing to hiatus-free  
631 deep-water sections.

632 Consequently, because (i) the presence of a stratigraphic hiatus in some sections will  
633 inevitably generate a spurious extinction event and (ii) conodont IZs across a depth gradient  
634 ranging from lagoonal to basinal depositional settings can hardly be synchronous, there is  
635 insufficient biostratigraphic evidence to support a second extinction event in South China.  
636 Consequently, it is concluded that the E2 Griesbachian Hg anomaly reported here is not  
637 associated with a second extinction pulse in South China.

#### 638 4.4 Provenance of volcanic Hg input

639 Our U-Pb geochronological results allow us to place the Pingtang syncline Hg record  
640 within the temporal framework of Siberian Traps Large Igneous Province magmatism (Burgess  
641 & Bowring, 2015; Burgess et al., 2017), a prominently discussed source of volatiles and toxic  
642 elements (such as Hg) during the Permian-Triassic transition (Black et al., 2012; Broadley et al.,  
643 2018; Sibik et al., 2021; Svensen et al., 2018). A maximum duration for intrusive and extrusive  
644 magmatic STLIP activity is given by the bracketing ages of  $252.27 \pm 0.11$  Ma (Burgess &  
645 Bowring, 2015) to  $250.60 \pm 0.22$  Ma (Augland et al., 2019), the latter from syenitic intrusions  
646 with an uncertain relationship to the STLIP. Therefore, STLIP magmatism, being active during  
647 the studied interval, is a potential source of volcanic Hg input to South China during the  
648 Permian-Triassic transition.

649 However, several studies have demonstrated that more proximal regional volcanic  
650 activity related to convergent plate tectonism and subduction magmatism occurred during the  
651 Permian-Triassic transition, which led to elevated Hg concentrations and may have contributed  
652 to the PTBME in South China (Gao et al., 2013; He et al., 2014; Jiao et al., 2022; H. Zhang et al.,  
653 2021; Zhao et al., 2019; Zheng et al., 2020). In addition to Hg/TOC anomalies close to the  
654 PTBME horizon, Hg/TOC excursions and corresponding Hg isotope compositions have been  
655 documented for the earliest Triassic (Griesbachian) from South China and northern India (Wang  
656 et al., 2019a, 2018). Wang et al. (2019a) documented a pair of Hg/TOC anomalies in the latest  
657 Permian and earliest Triassic respectively, accompanied by a decreasing trend of  $\Delta^{199}\text{Hg}$  values  
658 from the Changhsingian to the Griesbachian. Based on this  $\Delta^{199}\text{Hg}$  trend, they interpreted their  
659 Griesbachian Hg/TOC excursion as having resulted from terrestrial Hg input due to elevated  
660 Early Triassic continental weathering. Recently, J. Shen et al. (2021) reported several Hg  
661 enrichment intervals predating the PTBME (named ME1-ME3), as well as one interval coeval  
662 with the PTBME (ME4), from three marine sections in South China. These authors reported the  
663 same pattern of decreasing  $\Delta^{199}\text{Hg}$  values from the Changhsingian to Griesbachian. The Hg  
664 anomalies preceding the PTBME were interpreted to reflect regional subduction-related  
665 volcanism due to their spatial restriction to the Tethys region, the occurrence of numerous

666 volcanic ash layers in Upper Permian rocks across South China, and the geochemical  
667 composition of zircons in these ash layers supporting a subduction-zone volcanic arc origin.

668 In contrast with previous studies, the Hg MIF values ( $\Delta^{199}\text{Hg}$ ,  $\Delta^{200}\text{Hg}$ ) in the current  
669 study remain near-zero throughout the Changhsingian to Griesbachian (Fig. 7). This supports the  
670 inference of a constant, dominantly atmospheric volcanic Hg source. Furthermore, Hg shows no  
671 correlation to Al – a proxy for clastic input – in either locality (Fig. 4), arguing against terrestrial  
672 inputs as a major Hg source. The disparity between the Hg isotope MIF record of the Pingtang  
673 syncline and other deep-water marine records in South China (e.g., Wang et al., 2019a; J. Shen et  
674 al., 2021) (Fig. 8) suggests that Hg isotope compositions alone may not be sufficient for  
675 discriminating Hg sources to deep-water depositional sites during the Permian-Triassic transition  
676 in South China.

677 As the Hg excursions in the Pingtang syncline successions are recorded in strata with  
678 numerous interbedded volcanic ash layers, the major and trace element geochemical properties  
679 of these volcanic ashes can be used to trace the origin of volcanic Hg inputs to these successions.  
680 The analyzed volcanic ash beds from Potuo have major and trace element characteristics similar  
681 to previously studied volcanic ashes from South China (Fig. 6) (He et al., 2014; Wang et al.,  
682 2019b). Their primitive mantle-normalized trace element compositions (Sun & McDonough,  
683 1989) are characterized by depletions in Ta, Nb, Sr and Ti, similar to rocks from subduction  
684 settings (Pearce et al., 1995). The ashes show intermediate to acidic chemical compositions,  
685 plotting in the field of basaltic andesite, trachy-andesite and rhyolite/dacite (Fig. 6a), and are  
686 chemically distinct from volcanic rocks originating from the STLIP (Callegaro et al., 2021;  
687 Reichow et al., 2005; Sibik et al., 2015; Sobolev et al., 2009). In addition, a mid-oceanic ridge  
688 basalt (MORB)-normalized trace element (Th vs. Nb) discriminant plot (Saccani et al., 2015,  
689 2018) of the volcanic ashes from the Pingtang syncline suggests that they originate from a  
690 continental margin volcanic arc tectonic setting (Fig. 6b). Similar conclusions were reached for  
691 other volcanic ashes from successions straddling the PTB in South China, in that these ashes  
692 have no genetic link to the Siberian Traps, but instead derived from subduction zone arc  
693 volcanism in the Tethys region (Gao et al., 2013; He et al., 2014; Jiao et al., 2022; Song et al.,  
694 2022; Zhao et al., 2019).

695 Consequently, we conclude that episodic regional arc volcanism associated with  
696 convergent plate tectonics in the Tethys region can explain the elevated Hg input to the  
697 Nanpanjiang Basin as recorded in the Pingtang syncline during Changhsingian to Griesbachian  
698 times. Furthermore, based on general atmospheric circulation models, previous studies have  
699 suggested that the Canadian Arctic was favorably positioned to receive volatiles (including  
700 volcanic ash) from the STLIP during the Permian to Triassic because it was situated downwind  
701 relative to the location of the STLIP eruptions (Dal Corso et al., 2022; Grasby et al., 2011, 2013).  
702 In this scenario, the South China region, being located towards the southeast and several  
703 thousands of kilometers away from Siberia, would have been poorly situated to receive volatiles  
704 from the STLIP. Finally, as noted by J. Shen et al. (2023), volcanic arc magmatism along the  
705 eastern margin of the PaleoTethys was especially active during the Permian to Triassic, as  
706 inferred from abundant volcanic ash beds in coeval strata, as well as a number of associated Hg  
707 anomalies across the PTB in this region (Fig. 8).

#### 708 4.5 Hg anomalies, $\delta^{13}\text{C}$ excursions and volcanism during the P-T transition

709 Owing to the paucity of U-Pb zircon ages for deep-water sections from which Hg  
710 anomalies have been reported in South China, it is difficult to confidently correlate our recorded

711 Hg anomalies with those reported for other localities in the Tethys region. However, comparison  
712 of the Pingtang syncline Hg record with those published for other deep-water sections in South  
713 China, as well as shallower-water records (Meishan GSSP in South China and Guryul Ravine in  
714 northern India; Fig. 8), suggests that the minor E1 Changhsingian Hg anomaly may potentially  
715 correlate with the ME2 or ME3 episodes of J. Shen et al. (2021). These pre-PTB Hg anomalies  
716 are therefore recorded in both shallow and deep-water marine settings in South China. In  
717 contrast, the E2 Griesbachian Hg anomaly is not recorded from any shallow-water marine  
718 section nor deep-water sections in South China, except for deep-water sections in the  
719 Nanpanjiang Basin (e.g., Xinmin, Kejiao; Fig. 8). Nevertheless, E2 may be coeval with the Hg  
720 anomaly recorded between the *I. staeschei* and *I. isarcica* conodont zones (Wang et al., 2019a),  
721 which also coincides with the nadir of the PTB-straddling negative  $\delta^{13}\text{C}$  excursion in the  
722 southwestern Tethys Guryul Ravine section (Fig. 9). However, further work from other marine  
723 successions with precise U-Pb zircon ages is required to confirm the spatial extent of the  
724 Griesbachian Hg anomaly.

725 The (stratigraphically variable) coincidence of the nadir of  $\delta^{13}\text{C}$  excursions with Hg  
726 anomalies in the Pingtang syncline and other Tethyan successions (Fig. 9) hints at a common  
727 driving factor – volcanism. The global distribution of  $\delta^{13}\text{C}$  excursions and Hg anomalies close to  
728 the PTB in Permian-Triassic successions (Baud et al., 1996; Korte & Kozur, 2010; J. Shen et al.,  
729 2019) argues in favor of a large-scale volcanic degassing episode, such as that of the STLIP, as  
730 the ultimate cause of drastic environmental changes of global extent. The onset of the negative  
731  $\delta^{13}\text{C}$  excursion in the Pingtang syncline starts just before deposition of the ash layer (LAX8T) at  
732  $252.07 \pm 0.130$  Ma (Fig. 7) and is characterized by an initial 2 ‰ decrease in  $\delta^{13}\text{C}$  values in the  
733 upper Changhsingian followed by a further 3 ‰ decrease in the lower Griesbachian. This onset  
734 of  $\delta^{13}\text{C}$  excursion may temporally overlap with the transition from the extrusive Stage 1 to  
735 intrusive Stage 2 of STLIP magmatism, proposed to have occurred at about 251.9 Ma (Burgess  
736 et al., 2017). Stage 2 STLIP magmatism was characterized by intrusion of dykes and sills into  
737 country rocks in the Tunguska Basin (Burgess & Bowring, 2015; Burgess et al., 2017). The  
738 intrusions and subsequent sill complex formation is proposed to have caused injection of massive  
739 amounts of both  $\text{CO}_2$  and  $\text{CH}_4$  into the atmosphere via contact metamorphism of coal beds in the  
740 Tunguska Basin (Burgess et al., 2017; Svensen et al., 2009, 2018), which collectively are thought  
741 to result in a  $> 5$  ‰ negative  $\delta^{13}\text{C}$  excursion.

742 However, Davydov (2021) recently questioned the validity of this sill-rock thermal  
743 interaction model, pointing out that there is no correlation between coal metamorphism and the  
744 distribution of sills in the Tunguska Basin. This author also argued that the role of contact  
745 metamorphism by undifferentiated intrusions, which constitute  $> 95$  % of the Tunguska Basin  
746 intrusions, was limited and insignificant to the general coal metamorphism in the Tunguska  
747 Basin; and that coal metamorphism in the Tunguska Basin was probably related to regional  
748 tectonic deformation instead of magmatism. Furthermore, the role of intrusive STLIP  
749 magmatism as a potential driver of the global carbon cycle perturbations and mass extinction  
750 during the Permian-Triassic transition is questioned. This stems from the uncertainty regarding  
751 the age of the explosion pipes in the Tunguska Basin (which could have transported  $\text{CO}_2$  and  
752 other gases to the atmosphere), as well as the U-Pb ages of the sill intrusions that violate  
753 stratigraphic superposition (Davydov, 2021). Consequently, additional U-Pb zircon  
754 geochronologic calibrations of STLIP intrusive rocks are required to resolve these questions.

755 Pending the resolution of these questions, an additional but not mutually exclusive  
756 explanation that could reconcile the coincidence of negative  $\delta^{13}\text{C}$  excursions and Hg anomalies

757 recorded at a global scale during the Permian-Triassic transition can be considered. This is that  
758 concurrent regional arc volcanism in different palaeocontinents was responsible for both CO<sub>2</sub>  
759 and Hg release resulting in the δ<sup>13</sup>C excursions and Hg anomalies. In addition to South China,  
760 extensive regional arc volcanism during the Permian-Triassic transition has been documented for  
761 many spatially disparate localities. Some of these include: the northern Patagonian Massif,  
762 Argentina (Luppo et al., 2018), Antarctica (Nelson & Cottle, 2019), Sydney Basin, Australia  
763 (Metcalf et al., 2015), Karoo Basin, South Africa (Gastaldo et al., 2020), with coeval Hg  
764 anomalies also recently documented for the latter two (J. Shen et al., 2023). The suggestion of  
765 concurrent regional arc volcanism in several paleocontinents during the Permian-Triassic  
766 transition is congruent with recent suggestions of a Pangean ‘ring of fire’ (subduction-related  
767 volcanism along the convergent Panthalassan margin of Pangea) as an explanation for marine  
768 and terrestrial environmental perturbations during the latest Permian (Vajda et al., 2020).

769 Reasons for a global increase in regional arc volcanism concurrent with STLIP volcanism  
770 are still uncertain. Jiao et al. (2022) recently suggested that the ascent of the STLIP mantle plume  
771 may have triggered volcanic activity in several subduction zone systems. While the effect of a  
772 large mantle plume on global plate tectonics is highly debatable, STLIP volcanism occurred in a  
773 context of global increase of accretion and subduction rates from the Permian to Triassic (Vérard  
774 et al. 2015a, their Fig. 11a), which has also been linked with Early Triassic sea-level rise (Vérard  
775 et al., 2015b, their Fig. 17). However, such global increase in subduction rates is likely to occur  
776 over tens of millions of years. Hence, increased regional arc volcanism over hundreds of  
777 thousands of years between the latest Permian to earliest Triassic may be totally disconnected  
778 from global tectonics. Irrespective of the reasons for this global increase in volcanic activity over  
779 the Permian-Triassic transition, our results from the Pingtang syncline suggest that volcanic  
780 activity linked to Hg anomalies and C-isotope excursion probably peaked between  $251.589 \pm$   
781  $0.052$  Ma and  $251.668 \pm 0.079$  Ma in the Nanpanjiang Basin, South China (Fig. 7).

#### 782 4.6 Implications for the PTBME

783 While it is generally accepted that STLIP magmatism exerted a major control on the  
784 global carbon budget and mercury cycle during the Paleozoic to Mesozoic transition, it is clear  
785 that South China was substantially influenced by nearby volcanic centers throughout the Late  
786 Permian to Triassic (He et al., 2014; H. Zhang et al., 2021). This is evident from the older and  
787 well-known Emeishan LIP (Huang et al., 2022), the occurrence of Permian-Triassic volcanic  
788 rocks especially in southwest South China (Gao et al., 2013), the abundant volcanic ash layers  
789 within Permian-Triassic marine sedimentary successions, shown to be genetically distinct from  
790 STLIP rocks (Gao et al., 2013; He et al., 2014; Yang et al., 2012), as well as Changhsingian  
791 Hg/TOC anomalies restricted to the Tethys region (J. Shen et al., 2021; this study). The temporal  
792 overlap between regional intermediate to felsic volcanism and the basaltic volcanism from the  
793 STLIP, thus supports a scenario in which STLIP magmatism and concurrent subduction-related  
794 regional arc volcanism in the Tethys region may have acted in concert to generate pernicious  
795 environmental conditions for marine and terrestrial faunas in South China during the Late  
796 Permian. For example, the release of sulfur-rich volatiles from STLIP and regional volcanism  
797 may have triggered climatic cooling (Black et al., 2012; 2018; H. Zhang et al., 2021) leading to  
798 glacio-eustatic regression (Bagherpour et al., 2017; Baresel et al., 2017a), as well as ocean  
799 acidification during the latest Permian (Clarkson et al., 2015; Payne et al., 2010). Hence, the  
800 resultant loss of habitat due to shrunken marine shelves combined with ocean acidification may  
801 well have acted in concert to foster the PTBME in South China.

802 Furthermore, the finding of several sudden increases in mercury concentration that both  
803 predate and post-date the PTBME event is significant. This is because these Hg enrichments  
804 suggest that elevated volcanic activity, which is thought to have triggered the PTBME in South  
805 China, was not restricted only to a short interval e.g., within Stage 2 STLIP magmatism (Burgess  
806 et al., 2017), but rather, took place over several thousands of years during the Permian-Triassic  
807 transition. Thus, repeated bursts of regional felsic and intermediate volcanism (and resulting  
808 increases in mercury concentration) likely had a cumulative adverse effect on the environment  
809 and the species that lived at the time, making them more vulnerable to extinction, in agreement  
810 with similar suggestions by S. Shen et al. (2019). This provides further support for the inference  
811 that regional arc volcanism played a significant role in driving species to extinction in South  
812 China.

## 813 **5 Conclusions**

814 The present study establishes the Hg and  $\delta^{13}\text{C}$  record of two deep-water marine  
815 successions in the Nanpanjiang Basin, South China, spanning the Changhsingian to  
816 Griesbachian. U-Pb zircon ages and Hg/TOC ratios indicate elevated volcanic activity before  
817  $252.07 \pm 0.130$  Ma (preceding the PTBME) and during several episodes in the Griesbachian,  
818 peaking between  $251.589 \pm 0.052$  Ma and  $251.668 \pm 0.079$  Ma. The latter range in ages is coeval  
819 with the nadir of a large negative C isotope excursion, similar in magnitude to the global  
820 excursion at the PTB. Based on evidence from the coupled  $\delta^{13}\text{C}$  and Hg records, major and trace  
821 element geochemistry of volcanic ashes, and the U-Pb zircon age constraints, we conclude that  
822 the recorded Hg enrichments are primarily sourced from subduction-related arc volcanism in the  
823 Tethys region. Consequently, our Hg record together with recent results from South China  
824 documenting several episodes of Hg enrichment during the Permian-Triassic transition, highlight  
825 the role of regional volcanism with respect to regional faunal extinction. Our study provides an  
826 absolute timeframe within which Late Permian to Early Triassic Hg and  $\delta^{13}\text{C}$  records from  
827 different deep-water successions (which are less likely to contain stratigraphic gaps) in South  
828 China can be calibrated. This precise, radioisotopic timeframe allows for a more in-depth  
829 assessment of the relation between volcanism, environmental changes, and the mass extinction  
830 event at the Permian-Triassic transition.

## 831 **Acknowledgements**

832 This research was supported by a Swiss NSF Sinergia grant (project nr. CRSII5\_180253). We  
833 thank Olivier Reubi, Edson Ramudzuli and Jérôme Chmeleff for analytical assistance. Special  
834 thanks to Borhan Bagherpour and Marc Leu for providing logs for the study sections, and to  
835 members of the Sinergia PaleoC4 team for discussions during the development of this  
836 manuscript. The authors also thank Kuang Guodong (Geological survey of Guanxi), Ji Cheng  
837 (NIGPAS), Shen Shuzhong (University of Nanjing) for their help related to fieldwork and for  
838 scientific discussions.

## 839 **Conflict of interest**

840 The authors declare no conflict of interest relevant to this study.

## 841 **Author contributions**

842 Conceptualization & Funding acquisition: Hugo Bucher, Urs Schaltegger, Torsten Vennemann  
843 Formal analysis: Oluwaseun Edward, André N. Paul, Christian V  rard  
844 Investigation: Hugo Bucher, Oluwaseun Edward, Andr   N. Paul, Jeroen Sonke, Thierry Adate  
845 Resources: Urs Schaltegger, Thierry Adate, Jeroen Sonke, Torsten Vennemann  
846 Visualization: Oluwaseun Edward, Andr   N. Paul, Christian V  rard  
847 Writing – original draft: Oluwaseun Edward, Andr   N. Paul

#### 848 **Data availability Statement**

849 The dataset associated with the current study is available on the open-source online data  
850 repository – Zenodo – at “[*link-to-be-given-upon paper-acceptance*]”. Figure 1 was made based  
851 on the Panalesis model (V  rard, 2019) using ArcGIS  . Figures 2-8 were made with Matplotlib  
852 version 3.5.2 (Caswell et al., 2022), available under the Matplotlib license at  
853 <https://matplotlib.org>, and seaborn version 0.11.2 (Waskom, 2021) available at  
854 <https://pypi.org/project/seaborn/>. All figures were edited using Adobe Illustrator  .

#### 855 **References**

856 Augland, L. E., Ryabov, V. V., Vernikovsky, V. A., Planke, S., Polozov, A., Callegaro, S., et al.  
857 (2019). The main pulse of the Siberian Traps expanded in size and composition. *Scientific*  
858 *reports*, 9(1), 1-12. <https://doi.org/10.1038/s41598-019-54023-2>

859 Bagherpour, B., Bucher, H., Baud, A., Brosse, M., Vennemann, T., Martini, R., & Guodun, K.  
860 (2017). Onset, development, and cessation of basal Early Triassic microbialites (BETM) in the  
861 Nanpanjiang pull-apart Basin, South China Block. *Gondwana Research*, 44, 178-204.  
862 <https://doi.org/10.1016/j.gr.2016.11.013>

863 Bagherpour, B., Bucher, H., Vennemann, T., Schneebeli-Hermann, E., Yuan, D. X., Leu, M., et  
864 al. (2020). Are Late Permian carbon isotope excursions of local or of global significance?  
865 *Geological Society of America Bulletin*, 132(3-4), 521-544. <https://doi.org/10.1130/B31996.1>

866 Baresel, B., Bucher, H., Bagherpour, B., Brosse, M., Guodun, K., & Schaltegger, U. (2017a).  
867 Timing of global regression and microbial bloom linked with the Permian-Triassic boundary

- 868 mass extinction: implications for driving mechanisms. *Sci Rep*, 7, 43630.  
869 <https://doi.org/10.1038/srep43630>
- 870 Baresel, B., Bucher, H., Brosse, M., Cordey, F., Kuang, G. D., & Schaltegger, U. (2017b).  
871 Precise age for the Permian-Triassic boundary in South China from high-precision U-Pb  
872 geochronology and Bayesian age-depth modeling. *Solid Earth*, 8(2), 361-378.  
873 <https://doi.org/10.5194/se-8-361-2017>
- 874 Baud, A., Atudorei, V., & Sharp, Z. (1996). Late Permian and early Triassic evolution of the  
875 Northern Indian margin: Carbon isotope and sequence stratigraphy. *Geodinamica acta*, 9(2-3),  
876 57-77. <https://doi.org/10.1080/09853111.1996.11105278>
- 877 Baud, A., Magaritz, M., & Holser, W. T. (1989). Permian-Triassic of the Tethys: Carbon isotope  
878 studies. *Geologische Rundschau*, 78, 649-677. <https://doi.org/10.1007/BF01776196>
- 879 Behar, F., Beaumont, V., & Penteado, H. L. D. (2001). Rock-Eval 6 technology: Performances  
880 and developments. *Oil & Gas Science and Technology-Revue D Ifp Energies Nouvelles*, 56(2),  
881 111-134. <https://doi.org/10.2516/ogst:2001013>
- 882 Bergquist, B. A., & Blum, J. D. (2007). Mass-dependent and -independent fractionation of Hg  
883 isotopes by photoreduction in aquatic systems. *Science*, 318(5849), 417-420.  
884 <https://doi.org/10.1126/science.1148050>
- 885 Black, B. A., Elkins-Tanton, L. T., Rowe, M. C., & Peate, I. U. (2012). Magnitude and  
886 consequences of volatile release from the Siberian Traps. *Earth and Planetary Science Letters*,  
887 317, 363-373. <https://doi.org/10.1016/j.epsl.2011.12.001>
- 888 Black, B. A., Neely, R. R., Lamarque, J.-F., Elkins-Tanton, L. T., Kiehl, J. T., Shields, C. A., et  
889 al. (2018). Systemic swings in end-Permian climate from Siberian Traps carbon and sulfur  
890 outgassing. *Nature Geoscience*, 11(12), 949-954. <https://doi.org/10.1038/s41561-018-0261-y>

- 891 Blum, J. D., & Bergquist, B. A. (2007). Reporting of variations in the natural isotopic  
892 composition of mercury. *Anal Bioanal Chem*, 388(2), 353-359. [https://doi.org/10.1007/s00216-](https://doi.org/10.1007/s00216-007-1236-9)  
893 007-1236-9
- 894 Blum, J. D., Sherman, L. S., & Johnson, M. W. (2014). Mercury Isotopes in Earth and  
895 Environmental Sciences. *Annual Review of Earth and Planetary Sciences, Vol 42*, 42, 249-269.  
896 <https://doi.org/10.1146/annurev-earth-050212-124107>
- 897 Bowring, J. F., McLean, N. M., & Bowring, S. A. (2011). Engineering cyber infrastructure for  
898 U-Pb geochronology: Tripoli and U-Pb\_Redux. *Geochemistry Geophysics Geosystems*, 12(6).  
899 <https://doi.org/10.1029/2010gc003479>
- 900 Broadley, M. W., Barry, P. H., Ballentine, C. J., Taylor, L. A., & Burgess, R. (2018). End-  
901 Permian extinction amplified by plume-induced release of recycled lithospheric volatiles. *Nature*  
902 *Geoscience*, 11(9), 682-687. <https://doi.org/10.1038/s41561-018-0215-4>
- 903 Brosse, M., Bucher, H., & Goudemand, N. (2016). Quantitative biochronology of the Permian-  
904 Triassic boundary in South China based on conodont unitary associations. *Earth-Science*  
905 *Reviews*, 155, 153-171. <https://doi.org/10.1016/j.earscirev.2016.02.003>
- 906 Burgess, S. D., Bowring, S., & Shen, S. Z. (2014). High-precision timeline for Earth's most  
907 severe extinction. *Proc Natl Acad Sci U S A*, 111(9), 3316-3321.  
908 <https://doi.org/10.1073/pnas.1317692111>
- 909 Burgess, S. D., & Bowring, S. A. (2015). High-precision geochronology confirms voluminous  
910 magmatism before, during, and after Earth's most severe extinction. *Science advances*, 1(7),  
911 e1500470. <https://doi.org/10.1126/sciadv.1500470>

- 912 Burgess, S. D., Muirhead, J. D., & Bowring, S. A. (2017). Initial pulse of Siberian Traps sills as  
913 the trigger of the end-Permian mass extinction. *Nat Commun*, *8*(1), 164.  
914 <https://doi.org/10.1038/s41467-017-00083-9>
- 915 Callegaro, S., Svensen, H. H., Neumann, E. R., Polozov, A., Jerram, D. A., Deegan, F., et al.  
916 (2021). Geochemistry of deep Tunguska Basin sills, Siberian Traps: correlations and potential  
917 implications for the end-Permian environmental crisis. *Contributions to Mineralogy and*  
918 *Petrology*, *176*(7), 1-30. <https://doi.org/10.1007/s00410-021-01807-3>
- 919 Cao, C., Wang, W., & Jin, Y. (2002). Carbon isotope excursions across the Permian-Triassic  
920 boundary in the Meishan section, Zhejiang Province, China. *Chinese Science Bulletin*, *47*(13),  
921 1125-1129. <https://doi.org/10.1360/02tb9252>
- 922 Caswell, T. A., Droettboom, M., Lee, A., Sales De Andrade, E., Hoffmann, T., Klymak, J., et al.  
923 (2022). *Matplotlib v3.5.2*. In Zenodo. <https://doi.org/10.5281/zenodo.6513224>
- 924 Charbonnier, G., Adatte, T., Follmi, K. B., & Suan, G. (2020). Effect of Intense Weathering and  
925 Postdepositional Degradation of Organic Matter on Hg/TOC Proxy in Organic-rich Sediments  
926 and its Implications for Deep-Time Investigations. *Geochemistry Geophysics Geosystems*, *21*(2),  
927 e2019GC008707. <https://doi.org/10.1029/2019GC008707>
- 928 Charbonnier, G., Morales, C., Duchamp-Alphonse, S., Westermann, S., Adatte, T., & Föllmi, K.  
929 B. (2017). Mercury enrichment indicates volcanic triggering of Valanginian environmental  
930 change. *Scientific reports*, *7*(1), 1-6. <https://doi.org/10.1038/srep40808>
- 931 Chen, D., Ren, D., Deng, C., Tian, Z., & Yin, R. (2022). Mercury loss and isotope fractionation  
932 during high-pressure and high-temperature processing of sediments: Implication for the  
933 behaviors of mercury during metamorphism. *Geochimica et Cosmochimica Acta*, *334*, 231-240.  
934 <https://doi.org/10.1016/j.gca.2022.08.010>

- 935 Chen, J., Hintelmann, H., Feng, X., & Dimock, B. (2012). Unusual fractionation of both odd and  
936 even mercury isotopes in precipitation from Peterborough, ON, Canada. *Geochimica et*  
937 *Cosmochimica Acta*, *90*, 33-46. <https://doi.org/10.1016/j.gca.2012.05.005>
- 938 Clarkson, M., Kasemann, S. A., Wood, R., Lenton, T., Daines, S., Richoz, S., et al. (2015).  
939 Ocean acidification and the Permo-Triassic mass extinction. *Science*, *348*(6231), 229-232.  
940 <https://doi.org/10.1126/science.aaa0193>
- 941 Condon, D. J., Schoene, B., McLean, N. M., Bowring, S. A., & Parrish, R. R. (2015). Metrology  
942 and traceability of U-Pb isotope dilution geochronology (EARTHTIME Tracer Calibration Part  
943 I). *Geochimica et Cosmochimica Acta*, *164*, 464-480. <https://doi.org/10.1016/j.gca.2015.05.026>
- 944 Dal Corso, J., Song, H., Callegaro, S., Chu, D., Sun, Y., Hilton, J., et al. (2022). Environmental  
945 crises at the Permian–Triassic mass extinction. *Nature Reviews Earth & Environment*, *3*(3), 197-  
946 214. <https://doi.org/10.1038/s43017-021-00259-4>
- 947 Davydov, V. (2021). Tunguska coals, Siberian sills and the Permian-Triassic extinction. *Earth-*  
948 *Science Reviews*, *212*, 103438. <https://doi.org/10.1016/j.earscirev.2020.103438>
- 949 Fu, X., Jiskra, M., Yang, X., Maruszczak, N., Enrico, M., Chmeleff, J., et al. (2021). Mass-  
950 Independent Fractionation of Even and Odd Mercury Isotopes during Atmospheric Mercury  
951 Redox Reactions. *Environ Sci Technol*, *55*(14), 10164-10174.  
952 <https://doi.org/10.1021/acs.est.1c02568>
- 953 Gao, Q., Zhang, N., Xia, W., Feng, Q., Chen, Z.-Q., Zheng, J., et al. (2013). Origin of volcanic  
954 ash beds across the Permian–Triassic boundary, Daxiakou, South China: petrology and U–Pb  
955 age, trace elements and Hf-isotope composition of zircon. *Chemical Geology*, *360*, 41-53.  
956 <https://doi.org/10.1016/j.chemgeo.2013.09.020>

- 957 Gastaldo, R. A., Kamo, S. L., Neveling, J., Geissman, J. W., Looy, C. V., & Martini, A. M.  
958 (2020). The base of the Lystrosaurus Assemblage Zone, Karoo Basin, predates the end-Permian  
959 marine extinction. *Nature Communications*, *11*(1), 1-8. [https://doi.org/10.1038/s41467-020-](https://doi.org/10.1038/s41467-020-15243-7)  
960 [15243-7](https://doi.org/10.1038/s41467-020-15243-7)
- 961 Grasby, S. E., Sanei, H., & Beauchamp, B. (2011). Catastrophic dispersion of coal fly ash into  
962 oceans during the latest Permian extinction. *Nature Geoscience*, *4*(2), 104-107.  
963 <https://doi.org/10.1038/ngeo1069>
- 964 Grasby, S. E., Sanei, H., Beauchamp, B., & Chen, Z. H. (2013). Mercury deposition through the  
965 Permo-Triassic Biotic Crisis. *Chemical Geology*, *351*, 209-216.  
966 <https://doi.org/10.1016/j.chemgeo.2013.05.022>
- 967 Grasby, S. E., Shen, W. J., Yin, R. S., Gleason, J. D., Blum, J. D., Lepak, R. F., et al. (2017).  
968 Isotopic signatures of mercury contamination in latest Permian oceans. *Geology*, *45*(1), 55-58.  
969 <https://doi.org/10.1130/G38487.1>
- 970 Grasby, S. E., Them, T. R., Chen, Z. H., Yin, R. S., & Ardakani, O. H. (2019). Mercury as a  
971 proxy for volcanic emissions in the geologic record. *Earth-Science Reviews*, *196*, 102880.  
972 <https://doi.org/10.1016/j.earscirev.2019.102880>
- 973 Guex, J. (1991). *Biochronological correlations* (1 ed., Vol. 250). Springer Berlin, Heidelberg.  
974 [978-3-540-53937-7](https://doi.org/10.1007/978-3-540-53937-7)
- 975 Hammer, Ø., Jones, M. T., Schneebeli-Hermann, E., Hansen, B. B., & Bucher, H. (2019). Are  
976 Early Triassic extinction events associated with mercury anomalies? A reassessment of the  
977 Smithian/Spathian boundary extinction. *Earth-Science Reviews*, *195*, 179-190.  
978 <https://doi.org/10.1016/j.earscirev.2019.04.016>

- 979 He, B., Zhong, Y. T., Xu, Y. G., & Li, X. H. (2014). Triggers of Permo-Triassic boundary mass  
980 extinction in South China: The Siberian Traps or Paleo-Tethys ignimbrite flare-up? *Lithos*, *204*,  
981 258-267. <https://doi.org/10.1016/j.lithos.2014.05.011>
- 982 Holland, S. M., & Patzkowsky, M. E. (2015). The stratigraphy of mass extinction.  
983 *Palaeontology*, *58*(5), 903-924. <https://doi.org/10.1111/pala.12188>
- 984 Huang, H., Huyskens, M. H., Yin, Q.-Z., Cawood, P. A., Hou, M., Yang, J., et al. (2022).  
985 Eruptive tempo of Emeishan large igneous province, southwestern China and northern Vietnam:  
986 Relations to biotic crises and paleoclimate changes around the Guadalupian-Lopingian boundary.  
987 *Geology*, *50*(9), 1083-1087. <https://doi.org/10.1130/G50183.1>
- 988 Jiao, Y., Zhou, L., Algeo, T. J., Shen, J., Feng, L., Hu, Y., et al. (2022). Zirconium isotopes track  
989 volcanic inputs during the Permian-Triassic transition in South China. *Chemical Geology*, *610*,  
990 121074. <https://doi.org/10.1016/j.chemgeo.2022.121074>
- 991 Jiskra, M., Heimbürger-Boavida, L. E., Desgranges, M. M., Petrova, M. V., Dufour, A., Ferreira-  
992 Araujo, B., et al. (2021). Mercury stable isotopes constrain atmospheric sources to the ocean.  
993 *Nature*, *597*(7878), 678-682. <https://doi.org/10.1038/s41586-021-03859-8>
- 994 Jiskra, M., Sonke, J. E., Agnan, Y., Helmig, D., & Obrist, D. (2019). Insights from mercury  
995 stable isotopes on terrestrial-atmosphere exchange of Hg(0) in the Arctic tundra. *Biogeosciences*,  
996 *16*(20), 4051-4064. <https://doi.org/10.5194/bg-16-4051-2019>
- 997 Joachimski, M. M., Lai, X., Shen, S., Jiang, H., Luo, G., Chen, B., et al. (2012). Climate  
998 warming in the latest Permian and the Permian-Triassic mass extinction. *Geology*, *40*(3), 195-  
999 198. <https://doi.org/10.1130/G32707.1>

- 1000 Johnson, D. L., Present, T. M., Li, M., Shen, Y., & Adkins, J. F. (2021). Carbonate associated  
1001 sulfate (CAS)  $\delta^{34}\text{S}$  heterogeneity across the End-Permian Mass Extinction in South China.  
1002 *Earth and Planetary Science Letters*, 574, 117172. <https://doi.org/10.1016/j.epsl.2021.117172>
- 1003 Korte, C., & Kozur, H. W. (2010). Carbon-isotope stratigraphy across the Permian-Triassic  
1004 boundary: A review. *Journal of Asian Earth Sciences*, 39(4), 215-235.  
1005 <https://doi.org/10.1016/j.jseaes.2010.01.005>
- 1006 Kwon, S. Y., Blum, J. D., Nadelhoffer, K. J., Dvonch, J. T., & Tsui, M. T.-K. (2015). Isotopic  
1007 study of mercury sources and transfer between a freshwater lake and adjacent forest food web.  
1008 *Science of the Total Environment*, 532, 220-229. <https://doi.org/10.1016/j.scitotenv.2015.06.012>
- 1009 Lehrmann, D. J., Stepchinski, L., Altiner, D., Orchard, M. J., Montgomery, P., Enos, P., et al.  
1010 (2015). An integrated biostratigraphy (conodonts and foraminifers) and chronostratigraphy  
1011 (paleomagnetic reversals, magnetic susceptibility, elemental chemistry, carbon isotopes and  
1012 geochronology) for the Permian–Upper Triassic strata of Guandao section, Nanpanjiang Basin,  
1013 south China. *Journal of Asian Earth Sciences*, 108, 117-135.  
1014 <https://doi.org/10.1016/j.jseaes.2015.04.030>
- 1015 Leu, M., Bucher, H., & Goudemand, N. (2019). Clade-dependent size response of conodonts to  
1016 environmental changes during the late Smithian extinction. *Earth-Science Reviews*, 195, 52-67.  
1017 <https://doi.org/10.1016/j.earscirev.2018.11.003>
- 1018 Leu, M., Bucher, H., Vennemann, T., Bagherpour, B., Ji, C., Brosse, M., & Goudemand, N.  
1019 (2022). A Unitary Association-based conodont biozonation of the Smithian–Spathian boundary  
1020 (Early Triassic) and associated biotic crisis from South China. *Swiss Journal of Palaeontology*,  
1021 141(1), 19. <https://doi.org/10.1186/s13358-022-00259-x>

- 1022 Luppo, T., de Luchi, M. G. L., Rapalini, A. E., Dopico, C. I. M., & Fanning, C. M. (2018).  
1023 Geochronologic evidence of a large magmatic province in northern Patagonia encompassing the  
1024 Permian-Triassic boundary. *Journal of South American Earth Sciences*, 82, 346-355.  
1025 <https://doi.org/10.1016/j.jsames.2018.01.003>
- 1026 McLean, N. M., Bowring, J. F., & Bowring, S. A. (2011). An algorithm for U-Pb isotope dilution  
1027 data reduction and uncertainty propagation. *Geochemistry Geophysics Geosystems*, 12(6).  
1028 <https://doi.org/10.1029/2010GC003478>
- 1029 Metcalfe, I., Crowley, J., Nicoll, R., & Schmitz, M. (2015). High-precision U-Pb CA-TIMS  
1030 calibration of Middle Permian to Lower Triassic sequences, mass extinction and extreme  
1031 climate-change in eastern Australian Gondwana. *Gondwana Research*, 28(1), 61-81.  
1032 <https://doi.org/10.1016/j.gr.2014.09.002>
- 1033 Nelson, D. A., & Cottle, J. M. (2019). Tracking voluminous Permian volcanism of the Choiyoi  
1034 Province into central Antarctica. *Lithosphere*, 11(3), 386-398. <https://doi.org/10.1130/11015.1>
- 1035 Payne, J. L., Turchyn, A. V., Paytan, A., DePaolo, D. J., Lehrmann, D. J., Yu, M., & Wei, J.  
1036 (2010). Calcium isotope constraints on the end-Permian mass extinction. *Proceedings of the*  
1037 *National Academy of Sciences*, 107(19), 8543-8548. <https://doi.org/10.1073/pnas.0914065107>
- 1038 Pearce, J. A. (1982). Trace element characteristics of lavas from destructive plate boundaries. In  
1039 R. S. Thorpe (Ed.), *Orogenic andesites and related rocks* (pp. 528-548). John Wiley and Sons.  
1040 9780471280347
- 1041 Pearce, J. A., Baker, P. E., Harvey, P. K., & Luff, I. W. (1995). Geochemical evidence for  
1042 subduction fluxes, mantle melting and fractional crystallization beneath the South Sandwich  
1043 island arc. *Journal of Petrology*, 36(4), 1073-1109. <https://doi.org/10.1093/petrology/36.4.1073>

- 1044 Portnyagin, M. V., Ponomareva, V. V., Zelenin, E. A., Bazanova, L. I., Pevzner, M. M.,  
1045 Plechova, A. A., et al. (2020). TephraKam: geochemical database of glass compositions in tephra  
1046 and welded tuffs from the Kamchatka volcanic arc (northwestern Pacific). *Earth System Science*  
1047 *Data*, 12(1), 469-486. <https://doi.org/10.5194/essd-12-469-2020>
- 1048 Pyle, D. M., & Mather, T. A. (2003). The importance of volcanic emissions for the global  
1049 atmospheric mercury cycle. *Atmospheric Environment*, 37(36), 5115-5124.  
1050 <https://doi.org/10.1016/j.atmosenv.2003.07.011>
- 1051 Reichow, M. K., Saunders, A. D., White, R. V., Al'Mukhamedov, A. I., & Medvedev, A. Y.  
1052 (2005). Geochemistry and petrogenesis of basalts from the West Siberian Basin: an extension of  
1053 the Permo–Triassic Siberian Traps, Russia. *Lithos*, 79(3), 425-452.  
1054 <https://doi.org/https://doi.org/10.1016/j.lithos.2004.09.011>
- 1055 S.Z. Shen, Ramezani, J., Chen, J., Cao, C. Q., Erwin, D. H., Zhang, H., et al. (2019). A sudden  
1056 end-Permian mass extinction in South China. *Geological Society of America Bulletin*, 131(1-2),  
1057 205-223. <https://doi.org/10.1130/B31909.1>
- 1058 Saccani, E., Delavari, M., Dolati, A., Marroni, M., Pandolfi, L., Chiari, M., & Barbero, E.  
1059 (2018). New insights into the geodynamics of Neo-Tethys in the Makran area: Evidence from  
1060 age and petrology of ophiolites from the Coloured Mélange Complex (SE Iran). *Gondwana*  
1061 *Research*, 62, 306-327. <https://doi.org/10.1016/j.gr.2017.07.013>
- 1062 Saccani, E., Dilek, Y., Marroni, M., & Pandolfi, L. (2015). Continental margin ophiolites of  
1063 Neotethys: remnants of ancient Ocean–Continent Transition Zone (OCTZ) lithosphere and their  
1064 geochemistry, mantle sources and melt evolution patterns. *Episodes Journal of International*  
1065 *Geoscience*, 38(4), 230-249. <https://doi.org/10.18814/epiiugs/2015/v38i4/82418>

- 1066 Sanei, H., Grasby, S. E., & Beauchamp, B. (2012). Latest Permian mercury anomalies. *Geology*,  
1067 *40*(1), 63-66. <https://doi.org/10.1130/G32596.1>
- 1068 Schaltegger, U., Ovtcharova, M., Gaynor, S. P., Schoene, B., Wotzlaw, J.-F., Davies, J. F., et al.  
1069 (2021). Long-term repeatability and interlaboratory reproducibility of high-precision ID-TIMS  
1070 U–Pb geochronology. *Journal of Analytical Atomic Spectrometry*, *36*(7), 1466-1477.  
1071 <https://doi.org/10.1039/D1JA00116G>
- 1072 Schoene, B., Crowley, J. L., Condon, D. J., Schmitz, M. D., & Bowring, S. A. (2006).  
1073 Reassessing the uranium decay constants for geochronology using ID-TIMS U-Pb data.  
1074 *Geochimica et Cosmochimica Acta*, *70*(2), 426-445. <https://doi.org/10.1016/j.gca.2005.09.007>
- 1075 Shen, J., Chen, J., Algeo, T. J., Feng, Q., Yu, J., Xu, Y.-G., et al. (2021). Mercury fluxes record  
1076 regional volcanism in the South China craton prior to the end-Permian mass extinction. *Geology*,  
1077 *49*(4), 452-456. <https://doi.org/10.1130/G48501.1>
- 1078 Shen, J., Chen, J., Algeo, T. J., Yuan, S., Feng, Q., Yu, J., et al. (2019). Evidence for a prolonged  
1079 Permian-Triassic extinction interval from global marine mercury records. *Nat Commun*, *10*(1),  
1080 1563. <https://doi.org/10.1038/s41467-019-09620-0>
- 1081 Shen, J., Chen, J., Yu, J., Algeo, T. J., Smith, R. M. H., Botha, J., et al. (2023). Mercury evidence  
1082 from southern Pangea terrestrial sections for end-Permian global volcanic effects. *Nature*  
1083 *Communications*, *14*(1), 6. <https://doi.org/10.1038/s41467-022-35272-8>
- 1084 Shen, J., Feng, Q. L., Algeo, T. J., Liu, J. L., Zhou, C. Y., Wei, W., et al. (2020). Sedimentary  
1085 host phases of mercury (Hg) and implications for use of Hg as a volcanic proxy. *Earth and*  
1086 *Planetary Science Letters*, *543*, 116333. <https://doi.org/10.1016/j.epsl.2020.116333>
- 1087 Shen, S.-z., Cao, C.-q., Zhang, H., Bowring, S. A., Henderson, C. M., Payne, J. L., et al. (2013).  
1088 High-resolution  $\delta^{13}\text{C}_{\text{carb}}$  chemostratigraphy from latest Guadalupian through earliest Triassic in

- 1089 South China and Iran. *Earth and Planetary Science Letters*, 375, 156-165.  
1090 <https://doi.org/10.1016/j.epsl.2013.05.020>
- 1091 Shen, S.-z., Crowley, J. L., Wang, Y., Bowring, S. A., Erwin, D. H., Sadler, P. M., et al. (2011).  
1092 Calibrating the end-Permian mass extinction. *Science*, 334(6061), 1367-1372.  
1093 <https://doi.org/10.1126/science.1213454>
- 1094 Sial, A. N., Chen, J. B., Lacerda, L. D., Korte, C., Spangenberg, J. E., Silva-Tamayo, J. C., et al.  
1095 (2020). Globally enhanced Hg deposition and Hg isotopes in sections straddling the Permian-  
1096 Triassic boundary: Link to volcanism. *Palaeogeography Palaeoclimatology Palaeoecology*, 540,  
1097 109537. <https://doi.org/10.1016/j.palaeo.2019.109537>
- 1098 Sibik, S., Edmonds, M., MacLennan, J., & Svensen, H. (2015). Magmas erupted during the main  
1099 pulse of Siberian Traps volcanism were volatile-poor. *Journal of Petrology*, 56(11), 2089-2116.  
1100 <https://doi.org/10.1093/petrology/egv064>
- 1101 Sibik, S., Edmonds, M., Villemant, B., Svensen, H. H., Polozov, A. G., & Planke, S. (2021).  
1102 Halogen enrichment of Siberian Traps magmas during interaction with evaporites.  
1103 <https://doi.org/10.3389/feart.2021.741447>
- 1104 Sobolev, A. V., Krivolutsкая, N. A., & Kuzmin, D. V. (2009). Petrology of the parental melts  
1105 and mantle sources of Siberian trap magmatism. *Petrology*, 17(3), 253-286.  
1106 <https://doi.org/10.1134/S0869591109030047>
- 1107 Song, H., Wignall, P. B., Tong, J., & Yin, H. (2013). Two pulses of extinction during the  
1108 Permian–Triassic crisis. *Nature Geoscience*, 6(1), 52-56. <https://doi.org/10.1038/ngeo1649>
- 1109 Song, Q., Hong, H., Algeo, T. J., Fang, Q., Zhao, C., Liu, C., & Xu, Y. (2022). Clay mineralogy  
1110 mediated by pH and chemical weathering intensity of Permian–Triassic boundary K-bentonites

- 1111 at Dongpan (Guangxi, South China). *Chemical Geology*, 121262.  
1112 <https://doi.org/10.1016/j.chemgeo.2022.121262>
- 1113 Sonke, J. E., Schafer, J., Chmeleff, J., Audry, S., Blanc, G., & Dupre, B. (2010). Sedimentary  
1114 mercury stable isotope records of atmospheric and riverine pollution from two major European  
1115 heavy metal refineries. *Chemical Geology*, 279(3-4), 90-100.  
1116 <https://doi.org/10.1016/j.chemgeo.2010.09.017>
- 1117 Sun, R., Enrico, M., Heimbürger, L. E., Scott, C., & Sonke, J. E. (2013). A double-stage tube  
1118 furnace--acid-trapping protocol for the pre-concentration of mercury from solid samples for  
1119 isotopic analysis. *Anal Bioanal Chem*, 405(21), 6771-6781. <https://doi.org/10.1007/s00216-013->  
1120 7152-2
- 1121 Sun, R., Streets, D. G., Horowitz, H. M., Amos, H. M., Liu, G., Perrot, V., et al. (2016).  
1122 Historical (1850–2010) mercury stable isotope inventory from anthropogenic sources to the  
1123 atmosphereMercury isotope emission inventory. *Elementa: Science of the Anthropocene*, 4.  
1124 <https://doi.org/10.12952/journal.elementa.000091>
- 1125 Sun, S.-S., & McDonough, W. F. (1989). Chemical and isotopic systematics of oceanic basalts:  
1126 implications for mantle composition and processes. *Geological Society, London, Special*  
1127 *Publications*, 42(1), 313-345. <https://doi.org/10.1144/GSL.SP.1989.042.01.1>
- 1128 Svensen, H., Planke, S., Polozov, A. G., Schmidbauer, N., Corfu, F., Podladchikov, Y. Y., &  
1129 Jamtveit, B. (2009). Siberian gas venting and the end-Permian environmental crisis. *Earth and*  
1130 *Planetary Science Letters*, 277(3-4), 490-500. <https://doi.org/10.1016/j.epsl.2008.11.015>
- 1131 Svensen, H. H., Frolov, S., Akhmanov, G. G., Polozov, A. G., Jerram, D. A., Shiganova, O. V.,  
1132 et al. (2018). Sills and gas generation in the Siberian Traps. *Philos Trans A Math Phys Eng Sci*,  
1133 376(2130), 20170080. <https://doi.org/10.1098/rsta.2017.0080>

- 1134 Thibodeau, A. M., & Bergquist, B. A. (2017). Do mercury isotopes record the signature of  
1135 massive volcanism in marine sedimentary records? *Geology*, 45(1), 95-96.  
1136 <https://doi.org/10.1130/focus012017.1>
- 1137 Thibodeau, A. M., Ritterbush, K., Yager, J. A., West, A. J., Ibarra, Y., Bottjer, D. J., et al.  
1138 (2016). Mercury anomalies and the timing of biotic recovery following the end-Triassic mass  
1139 extinction. *Nat Commun*, 7(1), 11147. <https://doi.org/10.1038/ncomms11147>
- 1140 Vajda, V., McLoughlin, S., Mays, C., Frank, T. D., Fielding, C. R., Tevyaw, A., et al. (2020).  
1141 End-Permian (252 Mya) deforestation, wildfires and flooding—an ancient biotic crisis with  
1142 lessons for the present. *Earth and Planetary Science Letters*, 529, 115875.  
1143 <https://doi.org/10.1016/j.epsl.2019.115875>
- 1144 V  rard, C., Hochard, C., Baumgartner, P. O., Stampfli, G. M., & Liu, M. (2015a). Geodynamic  
1145 evolution of the Earth over the Phanerozoic: Plate tectonic activity and palaeoclimatic indicators.  
1146 *Journal of Palaeogeography*, 4(2), 167-188. <https://doi.org/10.3724/SP.J.1261.2015.00072>
- 1147 V  rard, C., Hochard, C., Baumgartner, P. O., Stampfli, G. M., & Liu, M. (2015b). 3D  
1148 palaeogeographic reconstructions of the Phanerozoic versus sea-level and Sr-ratio variations.  
1149 *Journal of Palaeogeography*, 4(1), 64-84. <https://doi.org/10.3724/SP.J.1261.2015.00068>
- 1150 V  rard, C. (2019). Panalexis: towards global synthetic palaeogeographies using integration and  
1151 coupling of manifold models. *Geological Magazine*, 156(2), 320-330.  
1152 <https://doi.org/10.1017/S0016756817001042>
- 1153 Wang, X., Cawood, P. A., Zhao, H., Zhao, L., Grasby, S. E., Chen, Z.-Q., & Zhang, L. (2019a).  
1154 Global mercury cycle during the end-Permian mass extinction and subsequent Early Triassic  
1155 recovery. *Earth and Planetary Science Letters*, 513, 144-155.  
1156 <https://doi.org/10.1016/j.epsl.2019.02.026>

- 1157 Wang, X., Cawood, P. A., Zhao, L., Chen, Z.-Q., Lyu, Z., & Ma, B. (2019b). Convergent  
1158 continental margin volcanic source for ash beds at the Permian-Triassic boundary, South China:  
1159 Constraints from trace elements and Hf-isotopes. *Palaeogeography, Palaeoclimatology,*  
1160 *Palaeoecology*, 519, 154-165. <https://doi.org/10.1016/j.palaeo.2018.02.011>
- 1161 Wang, X. D., Cawood, P. A., Zhao, H., Zhao, L. S., Grasby, S. E., Chen, Z. Q., et al. (2018).  
1162 Mercury anomalies across the end Permian mass extinction in South China from shallow and  
1163 deep water depositional environments. *Earth and Planetary Science Letters*, 496, 159-167.  
1164 <https://doi.org/10.1016/j.epsl.2018.05.044>
- 1165 Waskom, M. L. (2021). Seaborn: statistical data visualization. *Journal of Open Source Software*,  
1166 6(60), 3021. <https://doi.org/10.21105/joss.03021>
- 1167 Widmann, P., Davies, J. H. F. L., & Schaltegger, U. (2019). Calibrating chemical abrasion: Its  
1168 effects on zircon crystal structure, chemical composition and U Pb age. *Chemical Geology*, 511,  
1169 1-10. <https://doi.org/10.1016/j.chemgeo.2019.02.026>
- 1170 Winchester, J. A., & Floyd, P. A. (1977). Geochemical discrimination of different magma series  
1171 and their differentiation products using immobile elements. *Chemical Geology*, 20, 325-343.  
1172 [https://doi.org/10.1016/0009-2541\(77\)90057-2](https://doi.org/10.1016/0009-2541(77)90057-2)
- 1173 Yager, J. A., West, A. J., Thibodeau, A. M., Corsetti, F. A., Rigo, M., Berelson, W. M., et al.  
1174 (2021). Mercury contents and isotope ratios from diverse depositional environments across the  
1175 Triassic-Jurassic Boundary: Towards a more robust mercury proxy for large igneous province  
1176 magmatism. *Earth-Science Reviews*, 223, 103775.  
1177 <https://doi.org/10.1016/j.earscirev.2021.103775>

- 1178 Yang, J., Cawood, P. A., Du, Y., Huang, H., Huang, H., & Tao, P. (2012). Large Igneous  
1179 Province and magmatic arc sourced Permian–Triassic volcanogenic sediments in China.  
1180 *Sedimentary Geology*, *261*, 120-131. <https://doi.org/10.1016/j.sedgeo.2012.03.018>
- 1181 Yin, H., Jiang, H., Xia, W., Feng, Q., Zhang, N., & Shen, J. (2014). The end-Permian regression  
1182 in South China and its implication on mass extinction. *Earth-Science Reviews*, *137*, 19-33.  
1183 <https://doi.org/10.1016/j.earscirev.2013.06.003>
- 1184 Yin, H., Zhang, K., Tong, J., Yang, Z., & Wu, S. (2001). The global stratotype section and point  
1185 (GSSP) of the Permian-Triassic boundary. *Episodes*, *24*(2), 102-114.  
1186 <https://doi.org/10.18814/epiiugs/2001/v24i2/004>
- 1187 Yuan, D.-X., Shen, S.-z., Henderson, C. M., Chen, J., Zhang, H., Zheng, Q.-f., & Wu, H. (2019).  
1188 Integrative timescale for the Lopingian (Late Permian): A review and update from Shangsi,  
1189 South China. *Earth-Science Reviews*, *188*, 190-209.  
1190 <https://doi.org/10.1016/j.earscirev.2018.11.002>
- 1191 Zambardi, T., Sonke, J. E., Toutain, J. P., Sortino, F., & Shinohara, H. (2009). Mercury  
1192 emissions and stable isotopic compositions at Vulcano Island (Italy). *Earth and Planetary  
1193 Science Letters*, *277*(1-2), 236-243. <https://doi.org/10.1016/j.epsl.2008.10.023>
- 1194 Zhang, G. J., Zhang, X. L., & Shen, Y. N. (2021). Quantitative constraints on carbon cycling and  
1195 temporal changes in episodic euxinia during the end-Permian mass extinction in South China.  
1196 *Chemical Geology*, *562*, 120036. <https://doi.org/10.1016/j.chemgeo.2020.120036>
- 1197 Zhang, H., Zhang, F., Chen, J. B., Erwin, D. H., Syverson, D. D., Ni, P., et al. (2021). Felsic  
1198 volcanism as a factor driving the end-Permian mass extinction. *Sci Adv*, *7*(47), eabh1390.  
1199 <https://doi.org/10.1126/sciadv.abh1390>

- 1200 Zhao, T. Y., Algeo, T. J., Feng, Q. L., Zi, J. W., & Xu, G. Z. (2019). Tracing the provenance of  
1201 volcanic ash in Permian-Triassic boundary strata, South China: Constraints from inherited and  
1202 syn-depositional magmatic zircons. *Palaeogeography Palaeoclimatology Palaeoecology*, 516,  
1203 190-202. <https://doi.org/10.1016/j.palaeo.2018.12.002>
- 1204 Zheng, B. S., Mou, C. L., Zhou, R. J., Wang, X. P., Xiao, Z. H., & Chen, Y. (2020). Nature and  
1205 origin of the volcanic ash beds near the Permian-Triassic boundary in South China: new data and  
1206 their geological implications. *Geological Magazine*, 157(4), 677-689.  
1207 <https://doi.org/10.1017/S001675681900133x>
- 1208 Zintwana, M. P., Cawthorn, R. G., Ashwal, L. D., Roelofse, F., & Cronwright, H. (2012).  
1209 Mercury in the Bushveld Complex, South Africa, and the Skaergaard Intrusion, Greenland.  
1210 *Chemical Geology*, 320, 147-155. <https://doi.org/10.1016/j.chemgeo.2012.06.001>